

NASA Contractor Report 3449

NASA  
CR  
3449  
c.1

0061974

TECH LIBRARY KAFB, NM

# Calculation of Vortex Lift Effect for Cambered Wings by the Suction Analogy

C. Edward Lan and Jen-Fu Chang

GRANT NSG-1629  
JULY 1981

LOAN COPY: RETURN TO  
APWL TECHNICAL LIBRARY  
KIRTLAND AFB, N.M.

**NASA**



## NASA Contractor Report 3449

# Calculation of Vortex Lift Effect for Cambered Wings by the Suction Analogy

C. Edward Lan and Jen-Fu Chang  
*The University of Kansas Center for Research, Inc.*  
*Lawrence, Kansas*

Prepared for  
Langley Research Center  
under Grant NSG-1629



National Aeronautics  
and Space Administration

**Scientific and Technical  
Information Branch**

1981

## Summary

An improved version of Woodward's chord plane aerodynamic panel method for subsonic and supersonic flow has been developed for cambered wings exhibiting edge-separated vortex flow, including those with leading-edge vortex flaps. The exact relation between leading-edge thrust and suction force in potential flow is derived. Instead of assuming the rotated suction force to be normal to wing surface at the leading edge, new orientation for the rotated suction force is determined through consideration of the momentum principle. The supersonic suction analogy method is improved by using an effective angle of attack defined through a semi-empirical method. Comparisons of predicted results with available data in subsonic and supersonic flow are presented.

## 1. INTRODUCTION

In references 1 and 2, an improved panel method was shown to be capable of predicting accurately the leading-edge and side-edge suction forces. In the method, a specific set of control point locations is obtained, based on a two-dimensional theory. All three-dimensional results presented for this method have been for non-cambered wings exhibiting edge-separated vortex flow. For highly swept cambered wings in subsonic compressible flow, a simplified method (as compared with that to be developed in this report) has been developed based on reference 3. That method uses the vortex-lattice method and suction analogy (VLM-SA) and is applicable only to subsonic flow. Its application to analysis and design of slender cambered wings has been reported in references 4 and 5.

It should be noted that in the existing suction analogy method, as exemplified by reference 3, the edge suction forces predicted for attached flow are rotated so that they are normal to the cambered wing surface along the leading and side edges to produce the vortex lift effect. This is a direct extension of Polhamus' suction analogy originally developed for a flat wing (reference 6). However, experimental evidence (references 7 and 8) indicates that the leading-edge vortex on a slender wing tends to migrate inboard as the angle of attack is increased. This implies that its suction force orientation depends on the local camber and the angle of attack, and is not always normal to the camber surface at the leading edge, as it is assumed in the existing method of suction analogy. Therefore, the migrating behavior of leading-edge vortex can not be predicted without modification of the current concept of suction analogy. In addition, the exact relation between the predicted thrust forces and edge suction forces has not been derived for a cambered wing.

The main purpose of this report is to present an improved method of suction analogy for slender cambered wings in subsonic and supersonic flow. The aforementioned deficiencies of the current method will be resolved, and comparison of experimental results with various existing methods for a variety of configurations will be given.

## 2. LIST OF SYMBOLS

$A$	aspect ratio
$b$	span
$c$	chord
$\bar{c}$	reference chord
$C_A$	total axial force coefficient
$C_{AV}$	axial force coefficient due to leading-edge vortex
$c_d$	sectional induced drag coefficient
$\Delta C_D$	$= C_D - (C_D)_{C_L=0}$ of non-cambered wings)
$C_{D_i}$	total near-field induced drag coefficient
$C_{D_{ii}}$	total far-field induced drag coefficient in attached flow
$c_l$	sectional lift coefficient
$C_L$	total lift coefficient
$C_{L_\alpha}$	lift-curve slope at small $\alpha$
$c_m$	sectional pitching moment coefficient about Y-axis
$C_m$	total pitching moment coefficient about Y-axis based on $\bar{c}$
$C_p$	pressure coefficient
$C_{p(PM)}$	pressure coefficient calculated by Prandtl-Meyer theory
$\Delta C_p$	lifting pressure coefficient
$c_s$	sectional leading-edge suction coefficient
$c_t$	sectional leading-edge thrust coefficient
$c_{tip}$	tip chord length
$\vec{i}, \vec{j}, \vec{k}$	unit vectors along X-, Y-, and Z-axes, respectively
$\vec{i}_s$	a unit vector normal to the wing leading edge (fig. 3)
$K_p$	planform lift curve slope per radian at $\alpha = 0^\circ$
$K_{v,le}$	leading-edge suction coefficient at one radian angle of attack
$K_{v,se}$	side-edge suction coefficient at one radian angle of attack

$K_\alpha$	an $\alpha$ -correction factor for the supersonic flow (eq. 54)
$M$	Mach number, or number of integration points
$\vec{n}$	a unit vector normal to the wing surface
$\vec{N}$	a normal vector
$N_c$	number of chordwise panels
$\vec{n}_\ell$	a unit normal vector to the wing surface at the leading edge
$N_s$	number of spanwise strips on right wing
$\vec{n}_\infty$	a unit vector normal to the freestream velocity vector
$r$	streamwise distance of suction force center from the leading edge as defined in figure 7. Radial distance in figure 6.
$\vec{r}$	position vector
$s$	local semi-span
$\vec{S}$	leading-edge suction force vector
$\vec{T}$	leading-edge thrust force vector
$\vec{t}_\ell$	a unit vector along the leading edge
$\vec{t}_\infty$	a unit vector along the freestream velocity vector
$u, v, w$	induced velocity components along X-, Y-, and Z-axes, respectively
$V$	velocity magnitude
$V_z$	z- component of velocity in the vortex flow field (figure 7)
$V_\theta$	circumferential velocity component in the vortex flow field (figure 7)
$x, y, z$	rectangular coordinates with positive X-axis along axis of symmetry pointing downstream, positive Y-axis pointing to right, and positive Z-axis pointing upward
$x_1, y_1, z_1$	a rectangular coordinate system obtained by rotating the XYZ system through an angle $\phi$ about X-axis
$x'_1, y'_1, z'_1$	a rectangular coordinate system obtained by translating the $X_1Y_1Z_1$ system along $Y_1$ -axis
$x_2, y_2, z_2$	a rectangular coordinate system obtained by rotating the $X_1Y_1Z_1$ system through an angle $\alpha_{tw}$ about $Y_1$ -axis

$x_l(y)$	x-coordinate of the leading edge
$z_c(x,y)$	camber surface ordinate measured from X-Y plane
$\bar{z}_c(x,y)$	camber surface ordinate measured from the mean chord plane
$z_l(y)$	z-coordinate of the leading edge measured from X-Y plane
$\alpha$	angle of attack
$\bar{\alpha}$	average local angle of attack including twist and camber
$\Delta\alpha$	angle of attack correction in supersonic flow (eq. 53)
$\alpha_{tw}(y)$	wing twist angle at y
$\beta$	$= \sin^{-1}(\frac{1}{M})$
$\Delta, \Delta_1, \Delta_2, \Delta_3$	percent of elemental panel chord by which a control point on a leading-edge panel is moved downstream. See equations (47) and (48)
$\delta$	deflection angle
$\delta_c$	$= \tan^{-1} \left( \frac{d\bar{z}_c}{dx_2} \right)$
$\gamma$	ratio of specific heats (=1.4 for air)
$\gamma_x$	streamwise vortex density
$\lambda$	taper ratio
$\Lambda$	leading-edge sweep angle
$\phi$	dihedral angle
$\phi_y$	$= \tan^{-1} (\partial \bar{z}_c / \partial y_2)$
$\sigma$	control surface
$d\vec{\tau}$	elemental area vector
$\theta$	$= \tan^{-1} \left( \frac{\partial z}{\partial x} \right)$

### Subscripts

f	flap
le, l	leading edge
p	potential flow
r	root
se	side edge or tip chord



te	trailing edge
vle	leading-edge vortex flow
vse	side-edge vortex flow
$\infty$	freestream

### 3. THEORETICAL DEVELOPMENT

For the present purpose, the wing is assumed to be thin, and is cambered and twisted. The flow field satisfies the linear compressible governing equation which is solved through the use of pressure doublets (references 1 and 2). To calculate the pressure distribution and other aerodynamic characteristics, the boundary condition of flow tangency must be satisfied. This condition and others will be developed in the following.

#### 3.1 Boundary Condition

Assume that the wing surface (fig. 1) can be described by

$$z = z_c(x, y) \quad (1)$$

where  $z_c(x, y)$  is the ordinate of camber surface measured from the X-Y plane.

Introduce a function  $f$  such that

$$f = z - z_c(x, y) \quad (2)$$

Therefore, a unit normal vector on the wing surface can be defined as

$$\vec{n} = \frac{\vec{\nabla}f}{|\vec{\nabla}f|} = \frac{-\frac{\partial z_c}{\partial x} \vec{i} - \frac{\partial z_c}{\partial y} \vec{j} + \vec{k}}{\sqrt{1 + \left(\frac{\partial z_c}{\partial x}\right)^2 + \left(\frac{\partial z_c}{\partial y}\right)^2}} \quad (3)$$

The boundary condition on the wing surface requires that the total velocity component normal to the surface should vanish. Hence,

$$[(V_\infty \cos \alpha + u) \vec{i} + v \vec{j} + (V_\infty \sin \alpha + w) \vec{k}] \cdot \vec{n} = 0 \quad (4)$$

Using equation (3), equation (4) can be expanded to give

$$[-V_\infty \cos \alpha \frac{\partial z_c}{\partial x} - v \frac{\partial z_c}{\partial y} + V_\infty \sin \alpha + w] / \sqrt{1 + \left(\frac{\partial z_c}{\partial x}\right)^2 + \left(\frac{\partial z_c}{\partial y}\right)^2} \approx 0 \quad (5)$$

where  $u$  is assumed small in comparison with  $V_\infty \cos \alpha$ .

To simplify equation (5), it is assumed that the pressure doublets are distributed on a mean chord plane which is defined to be a non-twisted plane inclined with a dihedral angle ( $\phi$ ) to the X-Y plane. Since conventionally

the airfoil camber is defined with respect to its chord line (denoted here as  $\bar{z}_c(x_2, y_2)$  and shown on fig. 2) and the twist angle ( $\alpha_{tw}$ ) is measured relative to the mean chord plane, it is convenient to express the camber slopes,  $\frac{\partial z_c}{\partial x}$  and  $\frac{\partial z_c}{\partial y}$ , in terms of  $\frac{d\bar{z}_c}{dx_2}$ ,  $\frac{d\bar{z}_c}{dy_2}$ ,  $\alpha_{tw}$  and  $\phi$  before equation (5) can be further simplified. This can be done through the following coordinate transformations. The original XYZ system is rotated about X-axis through an angle  $\phi$  (dihedral angle), resulting in the  $X_1Y_1Z_1$  system, and then is rotated through an angle  $\alpha_{tw}$  (twist angle) about the  $Y_1$  axis to result in the  $X_2Y_2Z_2$  system (fig. 1). In figure 1, the  $X'_1Y'_1Z'_1$  system is obtained from the  $X_1Y_1Z_1$  system by a translation along the  $Y_1$  axis, just as the  $X'_2Y'_2Z'_2$  system is related to the  $X_2Y_2Z_2$  system.

According to vector analysis, the results of such coordinate rotations can be obtained by a series of orthogonal transformations (p. 413, ref. 9). It is shown in appendix A that  $\frac{\partial z_c}{\partial x}$  can be written as:

$$\frac{\partial z_c}{\partial x} = \frac{-\sin \alpha_{tw} + \frac{d\bar{z}_c}{dx_2} \cos \alpha_{tw}}{\cos \phi \left( \cos \alpha_{tw} + \frac{d\bar{z}_c}{dx_2} \sin \alpha_{tw} \right)} \quad (6)$$

or,

$$\cos \phi \frac{\partial z_c}{\partial x} = \frac{-\sin \alpha_{tw} + \frac{d\bar{z}_c}{dx_2} \cos \alpha_{tw}}{\cos \alpha_{tw} + \frac{d\bar{z}_c}{dx_2} \sin \alpha_{tw}} \quad (7)$$

Similarly,  $\frac{\partial z_c}{\partial y}$  is given by

$$\frac{\partial z_c}{\partial y} = \frac{\sin \phi \cos \alpha_{tw} + \frac{d\bar{z}_c}{dy_2} \cos \phi}{\cos \phi \cos \alpha_{tw} - \frac{d\bar{z}_c}{dy_2} \sin \phi} \quad (8)$$

To simplify equation (5), note that the perturbed sidewash ( $v$ ) is of the first order in magnitude. Following the thin wing theory, only first order terms will be retained in equation (5). Therefore, only the zero

order in  $\frac{\partial z_c}{\partial y}$  as given by equation (8) will be retained. In equation (8),  $\alpha_{tw}$  and  $\frac{dz_c}{dy_2}$  are both regarded as small and of the first order in magnitude. Hence, if the denominator in equation (8) is expanded for small  $\frac{dz_c}{dy_2}$ , it can be easily shown that:

$$\frac{\partial z_c}{\partial y} \approx \tan \phi \quad (9)$$

Hence, equation (5) now becomes

$$\frac{w}{V_\infty} - \frac{v}{V_\infty} \tan \phi \approx \frac{\partial z_c}{\partial x} \cos \alpha - \sin \alpha \quad (10a)$$

or,

$$\frac{w}{V_\infty} \cos \phi - \frac{v}{V_\infty} \sin \phi \approx \cos \phi \frac{\partial z_c}{\partial x} \cos \alpha - \cos \phi \sin \alpha \quad (10b)$$

The left-hand side of equation (10b) represents the total induced velocity normal to the mean chord plane. Using this interpretation, equation (10b) is still applicable even if  $\phi = 90^\circ$ , where  $\cos \phi \frac{\partial z_c}{\partial x}$  will be replaced with equation (7).

### 3.2 Relation between Leading-Edge Thrust and Suction

After the lifting pressure distribution is calculated, the leading-edge thrust coefficient  $c_t$  (in the negative x-direction) can be determined by using the pressure distribution as described in references (1) and (2). To calculate the suction coefficient ( $c_s$ ) from  $c_t$ , the following steps are taken.

Let  $\vec{i}_s$  be the unit vector along which the leading-edge suction force ( $|\vec{S}|$ ) acts in attached potential flow,  $\vec{t}_\ell$  is a unit vector along the leading edge and  $\vec{n}_\ell$  is the unit vector normal to the wing surface at the leading edge. They are indicated in figure 3. It follows that:

$$\vec{i}_s = \vec{n}_\ell \times \vec{t}_\ell \quad (11)$$

where  $\vec{n}_\ell$  is given by equation (3) evaluated at the leading edge. To find  $\vec{t}_\ell$ , note that along the leading edge, equation (1) can be written as

$$z_\ell(y) = z_c(x, y), \quad x = x_\ell(y) \quad (12)$$

The position vector of any point along the leading edge can be written as

$$\vec{r}(y) = x_\ell(y)\vec{i} + y\vec{j} + z_\ell(y)\vec{k} \quad (13)$$

The tangent vector is determined from

$$\frac{d\vec{r}}{dy} = \frac{dx_\ell}{dy} \vec{i} + \vec{j} + \frac{dz_\ell}{dy} \vec{k} \quad (14)$$

where

$$\frac{dx_\ell}{dy} = \tan \Lambda \quad (15)$$

$$\frac{dz_\ell}{dy} = \frac{\partial z_c}{\partial x} \tan \Lambda + \frac{\partial z_c}{\partial y} \quad (16)$$

It follows that the unit tangent vector  $\vec{t}_\ell$  is given by

$$\vec{t}_\ell = \frac{d\vec{r}}{dy} / \left| \frac{d\vec{r}}{dy} \right| \quad (17)$$

where

$$\left| \frac{d\vec{r}}{dy} \right| = \sqrt{1 + \tan^2 \Lambda + \left( \frac{dz_\ell}{dy} \right)^2} \quad (18)$$

Substituting equations (3) and (17) into equation (11) results in

$$\begin{aligned} \vec{i}_s = \vec{n}_\ell \times \vec{t}_\ell &= \begin{vmatrix} \vec{i} & \vec{j} & \vec{k} \\ -\frac{\partial z_c}{\partial x} & -\frac{\partial z_c}{\partial y} & 1 \\ \tan \Lambda & 1 & \frac{dz_\ell}{dy} \end{vmatrix} \frac{1}{\sqrt{1 + \left( \frac{\partial z_c}{\partial x} \right)^2 + \left( \frac{\partial z_c}{\partial y} \right)^2} \left| \frac{d\vec{r}}{dy} \right|} \\ &= \left\{ \vec{i} \left[ -\frac{\partial z_c}{\partial y} \frac{dz_\ell}{dy} - 1 \right] + \vec{j} \left[ \frac{\partial z_c}{\partial x} \frac{dz_\ell}{dy} + \tan \Lambda \right] + \vec{k} \left[ -\frac{\partial z_c}{\partial x} + \frac{\partial z_c}{\partial y} \tan \Lambda \right] \right\} \\ &\quad / \sqrt{1 + \left( \frac{\partial z_c}{\partial x} \right)^2 + \left( \frac{\partial z_c}{\partial y} \right)^2} \left| \frac{d\vec{r}}{dy} \right| \end{aligned} \quad (19)$$

Since the suction force  $\vec{S}$  is in the direction of  $\vec{i}_s$  in attached potential flow and the thrust  $\vec{T}$  is the component of  $\vec{S}$  in the X-Z plane, it follows that

$$\vec{T} = |\vec{S}| \left\{ \vec{i} \left[ -\frac{\partial z_c}{\partial y} \frac{dz_\ell}{dy} - 1 \right] + \vec{k} \left[ -\frac{\partial z_c}{\partial x} + \frac{\partial z_c}{\partial y} \tan \Lambda \right] \right\} \sqrt{1 + \left( \frac{\partial z_c}{\partial x} \right)^2 + \left( \frac{\partial z_c}{\partial y} \right)^2} \left| \frac{d\vec{r}}{dy} \right| \quad (20)$$

Thus, from equation (20), the sectional leading-edge suction coefficient ( $c_s$ ) can be obtained from the sectional leading-edge thrust coefficient ( $c_t$ ) as follows:

$$c_s = c_t \frac{\sqrt{1 + \left( \frac{\partial z_c}{\partial x} \right)^2 + \left( \frac{\partial z_c}{\partial y} \right)^2} \left| \frac{d\vec{r}}{dy} \right|}{\left\{ \left[ -\frac{\partial z_c}{\partial x} \frac{dz_\ell}{dy} + 1 \right]^2 + \left[ -\frac{\partial z_c}{\partial x} + \frac{\partial z_c}{\partial y} \tan \Lambda \right]^2 \right\}^{1/2}} \quad (21)$$

where all quantities are evaluated at the leading edge,  $\partial z_c / \partial x$ ,  $\partial z_c / \partial y$  are given in equations (6) and (8), and  $\frac{dz_\ell}{dy}$  is given in equation (16).

### 3.3 Orientation of Rotated Suction Force

In the method of suction analogy (reference 6) for a plane wing, the suction force predicted in the attached potential flow theory is rotated by  $90^\circ$  so that it is normal to the wing surface to simulate the vortex lift effect. If the same concept is used for a cambered wing, such as a delta wing with conically cambered leading edge (reference 7), then the rotated suction force, being normal to the wing surface at the leading edge, would produce an increasingly large thrust component on the mean chord plane as angles of attack are increased. However, experimental data for a conically cambered wing (reference 7), reproduced in figure 4, indicate that at high angles of attack the locations of minimum pressure values will move inboard onto the planar portion of the wing. Since the experimental leading-edge vortex-induced suction force can be obtained by summing all vortex-induced suction pressure forces, the center of this suction force will also move inboard. Similar situation occurs on a delta wing with leading-edge vortex flap (ref. 8). This is seen in figure 5 from an examination of the axial force coefficient

( $C_A$ ) measured relative to the flat portion of the wing. The data show that  $C_A$  stops increasing at about 16-17 degrees of angle of attack, indicating the leading-edge vortex has migrated over to the flat wing portion (reference 8). Therefore, successful estimation of this suction force center is necessary for determining the appropriate orientation of the vortex force, as well as predicting the migrating behavior of the vortex.

To be able to determine the location of this suction force center, a concept other than the suction analogy is needed. One possible way is to use the linear momentum principle of fluid mechanics. To get some idea on the flow field surrounding the leading-edge vortex, experimental results of Earnshaw (reference 10) are reproduced in figure 6. The velocity distribution was measured on a plane perpendicular to the freestream at a typical longitudinal station. Examining the circumferential velocity on a line a-a (fig. 6), its magnitude is approximately equal to the freestream velocity in a region from the vortex center to the leading edge, quadrant I, while it is less (about half of the freestream velocity in an average sense) inboard of the vortex center, quadrant III. The reason for the higher circumferential velocity outboard of the vortex center is probably due to the stronger effects of the vortex sheet and the "potential" flow. By "potential" flow, it is meant to be the non-separated flow component associated with the boundary condition being satisfied across the lifting surface. The results are quite similar in three other planes at 30, 50, and 70 percent of the root chord. It should be noted that the velocity shown in figure 6 is the total circumferential velocity including both the potential and vortex flow effects. Since the circumferential velocity on line a-a inboard of the vortex center, quadrant III, can be assumed to be primarily due to the vortex effect, with the "potential" component being small, it is reasonable to assume that the vortex-induced normal velocity on line a-a is about

$0.5 V_{\infty}$ .

From the aforementioned observation and assumption, a proposed flow model for the present purpose is depicted in figure (7a), where  $V_z$  is taken as  $0.5 V_{\infty}$ . Since  $c_s c \frac{1}{2} \rho V_{\infty}^2$ , by the suction analogy, is the vortex force per unit span, a width of unity for a section A-A is taken as shown in figure (7b). Now, a control surface ( $\sigma$ ) is taken through the vortex center as shown in figure (7c). It is then assumed that the vortex force is equal to the vertical component of the force due to the momentum transfer through the control surface  $\sigma$ . It follows that

$$-c_s c \frac{1}{2} \rho V_{\infty}^2 = \int_{\sigma} \rho V_z (\vec{V} \cdot d\vec{\tau}) \quad (22)$$

From the assumption that  $V_z = \frac{1}{2} V_{\infty}$ , the volume flow rate  $|\vec{V} \cdot d\vec{\tau}|$  will be:

$$|\vec{V} \cdot d\vec{\tau}| = \frac{1}{2} V_z \cdot 1 \cdot r \quad (23)$$

Therefore,

$$\begin{aligned} -c_s c \frac{1}{2} \rho V_{\infty}^2 &= \int_{\sigma} (\rho V_{z_{in}} - \rho V_{z_{out}}) \vec{V} \cdot d\vec{\tau} \\ &= -2 \left( \rho \frac{1}{2} V_{\infty} \cdot \frac{1}{2} V_{\infty} \cdot 1 \cdot r \right) \end{aligned}$$

or,

$$r = c_s c \quad (24)$$

Equation (24) is used to locate the assumed center of the vortex force and hence, the associated local slope for the orientation of the suction force. If the estimated suction force center is downstream of trailing edge, the corresponding camber slope for the force orientation is assumed to be zero.

Although the present results for the location of vortex force center can be used to estimate the vortex contribution to pitching moment, unfortunately it is not possible to determine how the "potential" lifting pressure should be redistributed in order to estimate the "potential" contribution to pitching moment. Therefore, for the purpose of calculating pitching



moment, the vortex force will tentatively still be assumed to be at the leading edge, except that its orientation will be altered as discussed previously.

### 3.4 Pressure Distribution and Total Forces and Pitching Moment

The calculated longitudinal induced velocity ( $u$ ) is assumed to be along the camber surface. Since in the linearized theory of both compressible and incompressible flow, the pressure coefficient ( $C_p$ ) is related to  $u$  in the same expression:

$$C_p \cong -2 \frac{u}{V_\infty} \quad (25)$$

in the following the incompressible Bernoulli equation will be used to find a correction factor for high  $\alpha$  in  $C_p$ .

The magnitude of undisturbed flow velocity on the mean chord plane is  $V_\infty$ . By resolving this velocity along and normal to the camber surface, the components  $V_\infty \cos(\alpha + \alpha_{tw} - \delta_c)$  and  $V_\infty \sin(\alpha + \alpha_{tw} - \delta_c)$  can be obtained, as indicated in figure 8 for  $\alpha_{tw} = 0$ . It follows that the pressure coefficient ( $C'_p$ ) at any angles of attack can be obtained from:

$$\begin{aligned} C'_p &= 1 - \frac{1}{V_\infty^2} [(V_\infty \cos(\tilde{\alpha} - \delta_c) + u)^2 + (V_\infty \sin(\tilde{\alpha} - \delta_c) + w)^2] \\ &\cong -2 \cos(\tilde{\alpha} - \delta_c) u/V_\infty = C_p \cos(\tilde{\alpha} - \delta_c) \end{aligned} \quad (26)$$

where  $\delta_c = \tan^{-1}(dz_c/dx_2)$  and  $\tilde{\alpha} = \alpha + \alpha_{tw}$ . It follows that

$$\Delta C'_p = \cos(\tilde{\alpha} - \delta_c) \Delta C_p \quad (27)$$

where  $\Delta C_p$  is predicted by satisfying the boundary condition equation (10a).

Physically, equation (27) implies that the predicted vortex strength from the attached potential flow theory is allowed to interact with the free stream velocity component tangent to the camber surface to produce the lifting pressure ( $\Delta C'_p$ ) (reference 6).

For a cambered wing with or without dihedral, additional lifting pressure will be generated from the interaction of a freestream component with the streamwise vortex density ( $\gamma_x$ ), as shown in figure 9. Adding this component of lifting pressure to that given in equation (27) results in:

$$\Delta C_p'' = \cos(\tilde{\alpha} - \delta_c) \Delta C_p - 2\gamma_x \sin\alpha \sin(\phi + \phi_y), \quad \tilde{\alpha} = \alpha + \alpha_{tw} \quad (28)$$

$$\phi_y = \tan^{-1} \left( \frac{d\bar{z}_c}{dy_2} \right) \quad (29)$$

where  $\phi_y$  may be defined as "local dihedral" angle and may be different everywhere on the cambered wing. On the other hand, the geometric dihedral angle  $\phi$  is constant along  $y$  for a given cambered or noncambered wing panel. For a noncambered wing,  $\phi_y = 0$  but  $\phi$  may not be zero. Note that in the normal lifting condition,  $\gamma_x$  is positive; because when viewed as a vector, it is pointing in the downstream (i.e., positive X-axis) direction.

The lifting pressure ( $\Delta C_p''$ ) is acting normal to the local camber surface, i.e., in the  $\vec{n}$  direction. This pressure force will be decomposed into  $\vec{n}_\infty$  and  $\vec{t}_\infty$  directions to determine the lift and drag components, respectively, where (see fig. 10)

$$\vec{n}_\infty = -\sin\alpha \vec{i} + \cos\alpha \vec{k} \quad (30)$$

$$\vec{t}_\infty = \cos\alpha \vec{i} + \sin\alpha \vec{k} \quad (31)$$

Using equation (3) for  $\vec{n}$  and then determining  $\vec{n} \cdot \vec{n}_\infty$  and  $\vec{n} \cdot \vec{t}_\infty$ , it can be shown that

$$c_{l,p} = \frac{1}{c} \int_{x_{le}}^{x_{te}} \Delta C_p'' \left( \frac{\partial z_c}{\partial x} \sin\alpha + \cos\alpha \right) / \sqrt{1 + \left( \frac{\partial z_c}{\partial x} \right)^2 + \left( \frac{\partial z_c}{\partial y} \right)^2} dx \quad (32)$$

$$c_{d,p} = \frac{1}{c} \int_{x_{le}}^{x_{te}} \Delta C_p'' \left( -\frac{\partial z_c}{\partial x} \cos\alpha + \sin\alpha \right) / \sqrt{1 + \left( \frac{\partial z_c}{\partial x} \right)^2 + \left( \frac{\partial z_c}{\partial y} \right)^2} dx \quad (33)$$

To find the pitching moment, the  $\vec{j}$ -component of

$$(\Delta x \vec{i} + \Delta z \vec{k}) \times \frac{-\frac{\partial z}{\partial x} \vec{i} - \frac{\partial z}{\partial y} \vec{j} + \vec{k}}{\sqrt{1 + \left(\frac{\partial z}{\partial x}\right)^2 + \left(\frac{\partial z}{\partial y}\right)^2}}$$

is needed, where  $\Delta x$  and  $\Delta z$  are the moment arms of the pressure elements referenced to the coordinate system. It follows that

$$c_{m,p} = -\frac{1}{c^2} \int_{x_{le}}^{x_{te}} \Delta C_p'' (\Delta x + \Delta z \frac{\partial z}{\partial x}) \left/ \sqrt{1 + \left(\frac{\partial z}{\partial x}\right)^2 + \left(\frac{\partial z}{\partial y}\right)^2} \right. dx \quad (34)$$

The contribution of leading-edge vortex effect to the sectional aerodynamic characteristics follows the same types of expressions given in equations (32)-(34). Hence,

$$c_{l,vle} = c_s \left( \frac{\partial z}{\partial x} \sin \alpha + \cos \alpha \right) \left/ \sqrt{1 + \left(\frac{\partial z}{\partial x}\right)^2 + \left(\frac{\partial z}{\partial y}\right)^2} \right. \quad (35)$$

$$c_{d,vle} = c_s \left( -\frac{\partial z}{\partial x} \cos \alpha + \sin \alpha \right) \left/ \sqrt{1 + \left(\frac{\partial z}{\partial x}\right)^2 + \left(\frac{\partial z}{\partial y}\right)^2} \right. \quad (36)$$

$$c_{m,vle} = -\frac{c_s}{c} (\Delta x_{le} + \Delta z_{le} \frac{\partial z}{\partial x}) \left/ \sqrt{1 + \left(\frac{\partial z}{\partial x}\right)^2 + \left(\frac{\partial z}{\partial y}\right)^2} \right. \quad (37)$$

where  $\frac{\partial z}{\partial x}$  and  $\frac{\partial z}{\partial y}$  are to be evaluated in accordance with the discussions of Section 3.3, regarding vortex movement.

Finally, spanwise integration of sectional characteristics given in equations (32)-(34) and equations (35)-(37) will produce the total force and moment coefficients:

$$C_{L,p} = \frac{2}{S} \int_0^{b/2} c_{l,p} c \, dy \quad (38)$$

$$C_{D,p} = \frac{2}{S} \int_0^{b/2} c_{d,p} c \, dy \quad (39)$$

$$C_{m,p} = \frac{2}{Sc} \int_0^{b/2} c_{m,p} c^2 \, dy \quad (40)$$

$$C_{L,vle} = \frac{2}{S} \int_0^{b/2} c_{l,vle} c \, dy \quad (41)$$

$$C_{D,vle} = \frac{2}{S} \int_0^{b/2} c_{d,vle} c \, dy \quad (42)$$

$$C_{m,vle} = \frac{2}{Sc} \int_0^{b/2} c_{m,vle} c^2 \, dy \quad (43)$$

The above integration can be performed by applying the trapezoidal rule, as shown in reference 11.

The side-edge contribution to the vortex-lift effect can be obtained by resolving the side-edge suction force, which is normal to the camber surface along the side edge, into  $\vec{n}_\infty$  and  $\vec{t}_\infty$  directions to determine lift and drag components, respectively. They have similar forms as those in equations (35)-(36). The pitching moment contribution follows equation (37) closely. Thus,

$$C_{L,vse} = \frac{c_{tip}}{S} \int c_{s,se} \left( \frac{\partial z}{\partial x} \sin \alpha + \cos \alpha \right) \sqrt{1 + \left( \frac{\partial z}{\partial x} \right)^2 + \left( \frac{\partial z}{\partial y} \right)^2} \, dx \quad (44)$$

$$C_{D,vse} = \frac{c_{tip}}{S} \int c_{s,se} \left( -\frac{\partial z}{\partial x} \cos \alpha + \sin \alpha \right) \sqrt{1 + \left( \frac{\partial z}{\partial x} \right)^2 + \left( \frac{\partial z}{\partial y} \right)^2} \, dx \quad (45)$$

$$C_{m,vse} = -\frac{c_{tip}}{Sc} \int c_{s,se} \left( \Delta x_{se} + \Delta z_{se} \frac{\partial z}{\partial x} \right) \sqrt{1 + \left( \frac{\partial z}{\partial x} \right)^2 + \left( \frac{\partial z}{\partial y} \right)^2} \, dx \quad (46)$$

where the integration is performed over the tip chord and  $c_{s,se}$  is the local side-edge suction coefficient. The determination of side-edge suction coefficient  $c_{s,se}$  is discussed in references 2 and 12. The values of  $\frac{\partial z}{\partial x}$  and  $\frac{\partial z}{\partial y}$  in equations (44)-(46) are determined along the tip chord without assuming inboard movement of side-edge vortex. This is based on the assumption that on usual configurations  $\frac{\partial z}{\partial y}$  does not vary too much near the tip and  $c_{s,se}$  is usually much smaller than  $c_s$  along the leading edge so that the vortex center will be quite close to the side edge.

In appendix B, analytical expressions to describe the geometry of leading-edge plane flaps and conical camber are derived. A numerical

method for calculating  $\frac{\partial \bar{z}_c}{\partial y_2}$  from the prescribed camber ordinates is given in appendix C.

#### 4. NUMERICAL RESULTS AND DISCUSSIONS

The computer program used in references (1) and (2) serves as a basis for further development to account for all features developed in Section 3. The three-dimensional effects (called sweep effect in references (1) and (2)) on choice of control-point locations have been re-examined. Since large geometric dihedral angles are now allowed in the program, the accuracy of calculation for configurations with large dihedral in both attached flow and separated flow must be assessed. The results of this re-examination and assessment, along with cambered wing data comparisons will be presented and discussed next.

##### 4.1 Three-Dimensional Effects on Control-Point Locations

In the present constant pressure panel method, the control point on an elemental panel is chosen based on a two-dimensional consideration to match pressure values with those given by the exact thin airfoil theory. However, it is well known that for a wing with large sweep angles and/or small taper ratios, the outboard pressure distribution can be quite different from a two-dimensional shape. To account for this effect, it was proposed in reference 2 to move downstream the control points of the leading-edge panels by an additional amount in percent,  $\Delta$ , of the elemental panel chord, where,

$$\text{for } M < 1, \quad \Delta_1 = 0 \quad \text{for } \Lambda \leq 60^\circ \quad (47a)$$

$$\Delta_2 = 0.35(\Lambda - 60) \quad \text{for } \Lambda > 60^\circ \quad (47b)$$

$$\text{for } M \geq 1, \quad \Delta_1 = 3.0 \quad \text{for } \Lambda \leq 60^\circ \quad (47c)$$

$$\Delta_2 = 0.35(\Lambda - 60) \quad \text{for } \Lambda > 60^\circ \quad (47d)$$

$$\Delta = \Delta_1 + \Delta_2 \quad (47e)$$

Equation (47e) appeared to be accurate for highly swept wings ( $\Lambda \geq 70^\circ$ ) with any taper ratio examined in reference 2. However, for moderately swept wings ( $\Lambda < 70^\circ$ ) with zero taper ratio, the results may not be accurate. This is illustrated in table 1(a). The assessment of accuracy is based on the ratio of near-field to far-field induced drag coefficients,  $C_{D_i}/C_{D_{ii}}$ , in the attached flow solution (i.e. with 100% leading-edge thrust)(reference 13). This ratio should be as close to unity as possible. A value of less than 1.0 for  $C_{D_i}/C_{D_{ii}}$  implies that the predicted leading-edge suction is too large. This appears to be true for all cases in table 1(a), except case (2). Apparently, not only the taper ratio (see cases (1) and (3)), but also the aspect ratio (see cases (1) and (5)) will affect the accuracy of the attached flow solution. To improve the accuracy, the following empirical factor,  $\Delta_3$  in percent, was used for all M's:

$$\Delta_3 = 3.5 (1-\lambda)^3 \frac{4}{2+A} \quad (48a)$$

$$\Delta = \Delta_1 + \text{greater of } (\Delta_2, \Delta_3) \quad (48b)$$

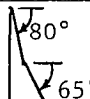
The aspect-ratio factor in equation (48a) was chosen such that for  $A = 2.0$ , the aspect-ratio factor is one. The results are presented in table 1(b) and appear to have significant improvement. Therefore, equation (48b) will be used in all following results. It should be noted that the adjustment represented by equation (48b) is applied to the outboard region of the wing only. For inboard regions, equation (47e) is still applicable.

#### 4.2 Effects of Dihedral Angles on Flat Wings

Effects of large dihedral angles on wing aerodynamic characteristics have been experimentally investigated in reference 14 with V-tails. In figures 11(a) and 11(b), the predicted results for two non-cambered V-tails in attached flow are compared with data. These tails are called in reference 14 Tail A and B and have aspect ratios of 5.55 and 3.70, respectively. Results by the quasi-vortex-lattice method (QVLM) (ref. 11) are also shown for the largest dihedral angles presented. The agreement between the present results

Table 1. Predicted Lift Factors and Induced Drag Ratio  
for Various Flat Configurations

(a) Present Method with equation (47e)

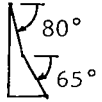
	Geometry	M	$K_p$	$K_{V,le}$	$K_{V,se}$	$C_{D_i}/C_{D_{ii}}^*$	Methods	$N_c \times N_s$
(1)	Delta	0.	3.16613	3.88620	0.	0.684	Present	10 x 12
	$\Lambda=50^\circ, \lambda=0.$		3.03177	3.18721	0.	1.087	ref. 11	7 x 12
(2)	Delta	0.	1.54912	2.95563	0.	1.0958	Present	10 x 12
	$\Lambda=74^\circ, \lambda=0.$		1.43638	2.93962	0.	1.0815	ref. 11	7 x 12
(3)	Delta	0.	2.94631	3.31705	0.20858	0.803	Present	10 x 12
	$\Lambda=50^\circ, \lambda=0.1$		2.86825	2.90379	0.20250	1.0423	ref. 11	7 x 12
(4)	Delta	0.7	2.54488	3.89359	0.	0.7755	Present	10 x 14
	$\Lambda=63.43^\circ, \lambda=0.$		2.39327	3.12126	0.	1.0814	ref. 11	10 x 14
(5)	Delta	0.	4.90702	4.49280	0.	0.8661	Present	7 x 15
	$\Lambda=20^\circ, \lambda=0.$		4.84672	4.28371	0.	1.0615	ref. 11	7 x 15
(6)	$\Lambda=45^\circ$	0.	1.63405	1.74318	0.38427	0.9216	Present	7 x 15
	$\Lambda=2.0, \lambda=0.5$		1.62226	1.68169	0.37001	1.0087	ref. 11	7 x 15
(7)		0.	1.83039	3.57093	0.	0.8179	Present	9 x 14
	same L.E. length in both regions		1.66340	3.03010	0.	1.1199	ref. 11	9 x 14

\* Attached flow results.



Table 1. (Concluded)

(b) Present Method with equation (48b)

	Geometry	M	$K_p$	$K_{V,le}$	$K_{V,se}$	$C_{D_i}/C_{D_{ii}}^*$	Methods	$N_c \times N_s$
(1)	Delta	0.	3.15358	3.19500	0.	1.135	Present	10 x 12
	$\Lambda=50^\circ, \lambda=0.$		3.03177	3.18721	0.	1.087	ref. 11	7 x 12
(2)	Delta	0.	1.54912	2.95563	0.	1.096	Present	10 x 12
	$\Lambda=74^\circ, \lambda=0.$		1.43638	2.93962	0.	1.0815	ref. 11	7 x 12
(3)	Delta	0.	2.93790	2.82564	0.20593	1.113	Present	10 x 12
	$\Lambda=50^\circ, \lambda=0.1$		2.86825	2.90379	0.2025	1.0423	ref. 11	7 x 12
(4)	Delta	0.7	2.53932	3.24207	0.	1.056	Present	10 x 14
	$\Lambda=63.43^\circ, \lambda=0.$		2.39327	3.12126	0.	1.0814	ref. 11	10 x 14
(5)	Delta	0.	4.88981	4.14896	0.	1.261	Present	7 x 15
	$\Lambda=20^\circ, \lambda=0.$		4.84672	4.28371	0.	1.0615	ref. 11	7 x 15
(6)	$\Lambda=45^\circ$	0.	1.63218	1.68857	0.38310	1.008	Present	7 x 15
	$A=2.0, \lambda=0.5$		1.62226	1.68169	0.37001	1.0087	ref. 11	7 x 15
(7)		0.	1.82592	3.10805	0.	1.055	Present	9 x 14
	same L.E. length in both regions		1.66340	3.03010	0.	1.1199	ref. 11	9 x 14

\* Attached flow results.

and those predicted by the QVLM is very good. The experimental data are all reasonably well predicted.

A nonplanar configuration exhibiting edge-separated vortex flow is shown in figure 12. The predicted aerodynamic characteristics are compared with experimental data (ref. 15) in figure 13. Several points are of interest.

(1) If the vortex lift is assumed to exist along all edges (i.e., full vortex lift curves), overall lift and drag are over-predicted. This has been verified in reference 15 with the conventional vortex-lattice method.

(2) If the outboard panel (identified as section II in fig. 13) is assumed not to carry vortex lift, but the leading-edge suction is also lost, the predicted results in  $C_L$  and  $C_D$  agree well with experimental data. This assumption is consistent with experimental observation that the organized vortex flow is weak on the outboard panel.

(3) The trend of variation due to tip dihedral is correctly predicted, i.e., increasing the tip dihedral reduces the  $C_L$  and  $C_D$ , and makes  $C_m$  more positive.

#### 4.3 Effect of $\frac{d\bar{z}_c}{dy_2}$ on Leading-Edge Suction Coefficient for Cambered Wings

Among the cambered wings examined so far, the delta wing with conical camber tested in reference 7 appears to be the most critical case in that along the leading edge the camber slopes amount to 0.3845 and -1.4402 for  $\frac{d\bar{z}_c}{dx_2}$  and  $\frac{d\bar{z}_c}{dy_2}$ , respectively. The camber geometry used in the present calculation is derived in appendix B. From numerical calculation, it was found that a large negative value of  $\frac{d\bar{z}_c}{dy_2}$  can greatly reduce the leading-edge suction

coefficient when equation (21) is directly used. (Note that  $\frac{\partial z_c}{\partial x}$ ,  $\frac{\partial z_c}{\partial y}$  and  $\frac{dz_l}{dy}$  in eq. (21) are related to  $\frac{d\bar{z}_c}{dx_2}$  and  $\frac{d\bar{z}_c}{dy_2}$  in eqs. (6), (8), and (16), respectively). This is illustrated in figure 14. It is seen that without

setting  $\frac{d\bar{z}_c}{dy_2}$  to zero in equation (21),  $c_{sc}$  is too low and hence the lift is underpredicted. This is perhaps because the boundary condition (eq. 10b) is applied on the mean chord plane and the doublet is distributed also on the same plane, instead of the actual camber surface. Because of the large magnitude of  $\frac{d\bar{z}_c}{dy_2}$  near the leading edge for this conically cambered wing, neglecting it will violate the small perturbation assumption in a small region near the leading edge. However, the present method is consistent with the usual practice in the thin wing theory. This means that  $\frac{d\bar{z}_c}{dy_2}$  has not been used in calculating the doublet strength. Therefore, in all calculations to be presented below,  $\frac{d\bar{z}_c}{dy_2}$  will be set to zero in equation (21).

#### 4.4 Effect of Vortex Force Orientation

Again, the conically cambered slender wing of reference 7 will be used to illustrate the effect of vortex force orientation. By setting  $r=0$  in equation (24), the vortex force will then be normal to the camber surface along the leading edge, an assumption being used in the existing methods. Figure 15 indicates that the present proposed theory ( $r = c_{sc}$ ) can significantly improve the predicted results. Therefore, all following calculations will correspond to  $r = c_{sc}$ .

As indicated in Section 3.3, the relation  $r = c_{sc}$  is mainly used to calculate the location for the vortex force orientation on a cambered wing. It is of interest to compare the location of vortex force centroid predicted by the present method with the leading-edge vortex location given by other methods. Figure 16 presents a comparison with the results by Brown and Michael in reference 16. The present method predicts the vortex force centroids slightly outboard of the vortex location given by reference 16. The model of Brown and Michael has further been employed in reference 17 where theoretical

results were compared with data for different planforms. The comparison indicated that the vortex force centroid shown in figure 16 by the present method and the vortex location by ref. 16 is too much outboard of the experimental vortex location. The same conclusion is true when compared with Smith's calculation (ref. 18). It should be noted that one additional effect included in reference 18, but not modelled in references 16 and 17, is the leading-edge free vortex sheet which is to increase the loading near the leading edge. This implies that the vortex force centroid will not coincide with the vortex location, but will be outboard of it. Therefore, the present method should be used only to find the vortex force centroid, but not the concentrated vortex-core location.

#### 4.5 Cambered Wings in Subsonic Flow

Several cambered slender wings have been used to correlate the predicted results with data. The results for the aforementioned conically cambered delta wing are compared with those by the vortex lattice method, VLM-SA, (ref. 3) in figure 17. The present results appear to agree better with data than those by VLM-SA in  $\Delta C_D$  and  $C_L$ . However, the difference in the predicted  $C_L$  is smaller than expected, despite of the fact that in VLM-SA the vortex force is assumed to be normal to the camber surface at the leading edge (see figure 15 for the effect). One possible reason is that in reference 3,  $\frac{\partial z_c}{\partial y}$  is taken to be zero in the denominator of equations (32) through (37), resulting in increased  $C_L$  and  $\Delta C_D$ . The predicted  $\Delta C_D$  at high angles of attack by the present method are slightly too low. Whether this is due to additional separation at the juncture of conical camber and the plane wing section is not known. On the other hand, the present pitching moment is too negative at high lift coefficient.

A highly cambered wing was tested by Squire and reported in reference 19. This wing has camber slopes,  $\frac{\partial z_c}{\partial x}$  and  $\frac{\partial z_c}{\partial y}$ , along the leading edge as high as

0.45 and -2.1, respectively. From the comparison made in figure 18,  $C_L$ ,  $\Delta C_D$  and  $C_m$  are all well predicted by both the present method and VLM-SA. The jump in experimental  $C_L$  at  $\alpha=20^\circ$  was explained in reference 19 to be due to merging of two vortices - one being the leading edge vortex and the other one being inboard vortex due to camber shoulder separation.

Recently, the use of leading-edge vortex flaps to increase the lift-drag ratio under maneuvering conditions has been of great interest. Some low speed results for a  $74^\circ$ -delta wing have been reported in reference 8. The geometry of the configuration used in the present method is shown in figure 19, where the dashed lines form the altered boundaries to define the planform in the present and VLM-SA computer programs. The undeflected trailing-edge flap on the test model is ignored for simplicity. The results are presented in figure 20. Note that all coefficients are based on total planform area excluding the flap. It is seen that the predicted results agree well with experimental data, as do those for the VLM-SA method. Note that the ability of the present method to predict the vortex force orientation makes it possible to estimate when the leading-edge vortex will move onto the plane wing. As shown in figure 21, the magnitude of vortex axial force coefficient ( $C_{AV}$ ) starts to drop at  $\alpha=16^\circ$ , implying that for  $\alpha > 16^\circ$  the vortex will migrate onto the wing. In reference 8, the  $\alpha$  at which this migration occurred was estimated to be  $17^\circ$ . The present results are therefore seen to be in good agreement with this reference.

Another configuration with full-span leading-edge flap was tested in 1958 at subsonic and supersonic speeds (ref. 20). The wing-body combination consists of a delta wing of aspect ratio 2.0 and NACA 0003-63 airfoil in the streamwise direction. The test results at  $M=0.7$  are compared in figure 22 with the predicted values for a configuration with the leading-edge flap

deflected down by 15 degrees normal to the hinge line. It is seen that the theoretical results by the present theory and VLM-SA agree quite well with the data. It should be noted that the fuselage in reference 20 is not modelled in either the present theory or the VLM-SA.

Two highly cambered wings designed by the method of vortex-lattice and suction analogy have been tested in subsonic flow. The results are presented in figures 23 and 24 together with theoretical prediction. It is seen from figure 23 that the present method offers significant improvement over VLM-SA in drag prediction. Presumably, this is due to the more accurate vortex force orientation calculated in the present method. For the cranked cambered wing shown in figure 24, the present predicted drag level is slightly too high at low  $C_L$ . The reason is not known. For  $C_L$  and  $C_m$ , the present results are in reasonably good agreement with data, except that the  $C_L$  for the cranked cambered wing is underpredicted at moderate angles of attack. These results are not, in general, any better than those of the VLM-SA with the exception of the  $C_D$  prediction.

#### 4.6 Wings in Supersonic Flow

##### Non-Cambered Wings

The method of suction analogy was first applied to delta wings in supersonic flow by Polhamus (ref. 22). If the concept is directly used on a delta wing of  $A = 4/3$ , results shown in figures 25 and 26 can be obtained. Note that the dashed curves denoted as the present theory without correction are the results by direct application of Polhamus' concept. So are the curves marked as original suction analogy. It is seen that the theory overpredicts  $C_L$  and underpredicts  $\Delta C_D$  slightly. Examination of the test cases in reference 22 indicates that the same trend persists on a delta wing of  $A = 1.0$  presented in that reference. Although the attached flow theory (with 100% leading-edge

suction) tends to predict  $C_L$  at low  $\alpha$  rather well, the drag is underpredicted. In addition, the test model used in reference 23 has sharp edges so that the concept of partial leading-edge suction investigated in reference 24 is not applicable. In an effort to improve the situation, it is helpful to study the flow field on a  $65^\circ$ -delta wing reported in reference 25. It was indicated in reference 25 that in supersonic flow the leading-edge separation starts at a higher angle of attack than that in subsonic flow on the same wing. The vortex flow region is diminished quickly as the Mach number is increased at a given angle of attack. In addition, the separated flow characteristics on a wing with small round leading edge (RAE 101 section) are quite similar to those with sharp leading edge (biconvex section). In fact, the longitudinal aerodynamic characteristics with fixed transition are practically the same for both airfoil sections. Since there is no doubt about the existence of separated vortex flow on slender wings in supersonic flow, the discrepancy between the results by current suction analogy and data must be nonlinear effect not accounted for in the linear potential flow theory. Of course, this conclusion is based on the assumption that the current suction analogy is still applicable in supersonic flow.

To find a correction to the linear potential flow theory, it is noted that the flow expansion on the suction side of the wing makes the vortex flow separation possible. Therefore, it is of interest to compare the suction pressure predicted by the linear theory with that given by the Prandtl-Meyer theory. In the two-dimensional case, it is shown in reference 26 (p. 386) that the linear theory predicts always a higher suction pressure. For a flat plate at an angle of attack  $\alpha$ , the upper surface pressure coefficient ( $C_p$ ) given by the linear theory is (ref. 26, p. 386)

$$C_p = - \frac{2\alpha}{\sqrt{M_\infty^2 - 1}} \quad (49)$$

On the other hand, the Prandtl-Meyer theory shows that (ref. 26, p. 383)

$$C_{p(PM)} = \frac{2}{\gamma M_\infty^2} \left[ \frac{\left( \frac{\sin^2 \beta}{\gamma - \cos 2\beta} \right)^{\frac{\gamma}{\gamma-1}}}{\left( \frac{\sin^2 \beta_\infty}{\gamma - \cos 2\beta_\infty} \right)^{\frac{\gamma}{\gamma-1}}} - 1 \right] \quad (50)$$

where  $\beta_\infty = \sin^{-1} \left( \frac{1}{M_\infty} \right)$  and  $\beta = \sin^{-1} \left( \frac{1}{M} \right)$  which must be found from (ref. 26, p. 377)

$$-\alpha + \beta - \sqrt{\frac{\gamma+1}{\gamma-1}} \tan^{-1} \left( \sqrt{\frac{\gamma+1}{\gamma-1}} \tan \beta \right) = \beta_\infty - \sqrt{\frac{\gamma+1}{\gamma-1}} \tan^{-1} \left( \sqrt{\frac{\gamma+1}{\gamma-1}} \tan \beta_\infty \right) \quad (51)$$

To make  $C_p = C_{p(PM)}$ , a correction ( $\alpha'$ ) to  $\alpha$  in equation (49) must be made such that

$$-\frac{2(\alpha + \alpha')}{\sqrt{M_\infty^2 - 1}} = C_{p(PM)}$$

or,

$$\alpha' = -\alpha - \frac{\sqrt{M_\infty^2 - 1}}{2} C_{p(PM)} \quad (52)$$

Equation (52) must be further modified based on the following two considerations. Firstly, equation (52) has been obtained by considering the upper surface pressure coefficient only, not the lifting pressure ( $\Delta C_p$ ). Assuming that the lower surface compression does not affect the upper surface vortex flow so that the linear theory prediction does not require modification, then the corresponding angle of attack correction to  $\Delta C_p$ ,  $\Delta\alpha$ , will be given by

$$\frac{4(\alpha + \Delta\alpha)}{\sqrt{M_\infty^2 - 1}} = \frac{2\alpha}{\sqrt{M_\infty^2 - 1}} + \frac{2(\alpha + \alpha')}{\sqrt{M_\infty^2 - 1}}$$

or,

$$\Delta\alpha = \frac{1}{2}\alpha'$$

Secondly, experimental evidence (ref. 25) indicated that as the Mach number is increased at a given  $\alpha$ , the vortex flow region will quickly diminish faster than predicted by reference 22. This means that  $\alpha'$  should decrease



in magnitude as  $M_\infty$  is increased. Presumably this is due to the three-dimensional effect, effect of conical shock above the vortex flow (ref. 25), etc. One simple way to account for these effects is to assume that  $\alpha'$  varies inversely with  $\sqrt{M_\infty^2 - 1}$ , in much the same way as  $C_p$  does (see eq. 49). A Mach number of 1.4 will be chosen as a reference (see below), because it is usually regarded as the lower bound in Mach number for the linear supersonic theory to be applicable. Combining the above considerations, the  $\alpha$ - correction,  $\Delta\alpha$ , can now be written as

$$\Delta\alpha = K_\alpha \left( -\alpha - \frac{\sqrt{M_\infty^2 - 1}}{2} C_{p(PM)} \right) \quad (53)$$

where

$$K_\alpha = \frac{1}{2} \quad , \quad M_\infty \leq 1.4 \quad (54a)$$

$$= \frac{1}{2} \frac{\sqrt{1.4^2 - 1}}{\sqrt{M_\infty^2 - 1}} \quad , \quad M_\infty > 1.4 \quad (54b)$$

Equation (53) is illustrated in figure 27 with and without equation (54b) for  $\alpha = 10$  deg. The magnitude of  $\Delta\alpha$  for different  $M_\infty$  and  $\alpha$  by equations (53), (54a) and (54b) is indicated in figure 28.

The results of applying  $\Delta\alpha$  correction to the calculation for a delta wing of aspect ratio 4/3 have also been presented in figures 25 and 26 for  $M_\infty = 1.4$  and 1.8. It is seen that a significant improvement in prediction is apparent.

In reference 22, the results by the original suction analogy method were compared with data from reference 27 for a delta wing of aspect ratio of 1.0 at  $M_\infty = 1.97$ . This comparison is reproduced in figure 29. It is seen that the lift is overpredicted and the drag at a given lift is underpredicted by the original method. On the other hand, the present modified method predicts both the lift and the drag quite well.

A slightly cropped delta wing of  $76^{\circ}$  sweep angle has been tested in supersonic flow with results reported in reference 28. The plane wing had 4-percent-thick circular arc airfoils. The test data are compared with the theoretical prediction in figure 30. In the present theory, if the side-edge (SE) vortex lift effect is included, the lift will be slightly overpredicted (about 4% at  $\alpha = 20$  deg.) and the drag slightly underpredicted. The pitching moment is slightly more negative at high  $C_L$  than the data show. On the other hand, if the side-edge vortex lift effect is ignored, good agreement between theory and data can be achieved. Whether this is true for wings with higher taper ratios is not known, since most available data were obtained on wings with zero or rather small taper ratios. The results by the Middleton-Carlson linear theory are also shown in figure 30. It underpredicts the lift at high  $\alpha$ 's and overpredicts the drag slightly.

Finally, the results for the cropped plane delta wing of  $65^{\circ}$  sweep angle reported in reference 25 are presented in figure 31. The fuselage is not modelled in the present program. It is seen that the theory with full vortex effect overpredicts  $C_L$  by about 10% at  $\alpha = 10$  deg. Excluding the side-edge vortex lift effect does not improve too much the agreement. One possible reason for the discrepancy is the presence of a fuselage which has a diameter-to-wing span ratio of 0.2083, and has a forward portion of  $0.75b$  ahead of wing root chord. Squire (ref. 25) observed that the fuselage tends to increase the angle of attack at which the vortex flow becomes significant. The main cause is the conical shock from the fore body. From figure 31, it is shown that the present theory with the potential flow component only (0% leading-edge suction) seems to predict the results rather well. The good agreement in this case may be fortuitous.

Further investigation of the fore body effect in supersonic flow is needed.

### Cambered Wings

For cambered wings, equation (53) should be modified by using some average local  $\alpha$ :

$$\Delta\alpha = K_{\alpha} \left( -\bar{\alpha} - \frac{\sqrt{M_{\infty}^2 - 1}}{2} C_{p(PM)} \right) \quad (55)$$

where  $K_{\alpha}$  is still given by equations (54). In the following calculation,  $\bar{\alpha}$  is assumed to be the arithmetic mean of local  $\alpha$  including twist and camber at all control points.

Several configurations of leading-edge flaps have been tested at  $M_{\infty} = 1.4$  and 1.8 and reported in reference 23. Results for deflection angles of 36.45 degrees and 60 degrees are presented in figures 32 and 33. It is seen that the lift is well predicted in all cases, in particular at  $M_{\infty} = 1.8$ . At a transonic Mach number of 1.4, the predicted  $C_L$  is slightly higher, with discrepancy being 8% or less. However, in all cases the drag is underpredicted for positive  $C_L$  and overpredicted for negative  $C_L$ . The same situation has been demonstrated in reference 30 (fig. 4C of that reference) for a configuration with leading-edge flaps deflected 20 deg. Possible reasons for this are flap hinge separation at positive  $C_L$  as indicated by the author in reference 23 and the nonlinear effect on wave drag. At negative lift, the drag data fall between the results for attached flow (100% leading-edge suction) and vortex flow. Whether this implies partial leading-edge vortex flow on the lower surface is not known.

To avoid the effect of possible leading-edge flap separation, a smoothly cambered wing would be more suitable to test the theory. Data of such a wing are available in reference 28 for a wing designed to cruise at  $M_{\infty} = 3.5$  and design  $C_L$  of 0.1. The results are presented in figure 34.

Again, the present theory without the side-edge vortex lift effect appears to be more accurate for  $C_L$  and  $\Delta C_D$ . However, it gives less accurate results for  $C_m$  at high  $C_L$ .

## CONCLUDING REMARKS

An aerodynamic panel program has been developed for cambered wings exhibiting edge-separated vortex flow at subsonic and supersonic speeds. Semi-empirical but simple methods have been developed to determine the appropriate position and hence orientation of vortex force on cambered wings, as well as to improve the prediction in supersonic flow. Comparison with available data indicates that (1) the program is accurate in predicting subsonic aerodynamic characteristics of highly cambered wings with vortex separation effect. The improvement in drag prediction over currently available methods can be significant. (2) The program is also accurate in predicting supersonic aerodynamic characteristics of slender wings with vortex separation. This has been achieved by employing an effective angle of attack in the suction analogy method.

In view of the improvement made in the present prediction method and possible further refinement, it would be of interest to:

- (1) use the program to design a supersonic wing so as to make efficient use of the vortex flow;
  - (2) examine the fuselage effect on wing vortex flow more closely;
  - (3) reexamine the drag associated with using leading-edge flaps in supersonic flow;
- and (4) make additional verification studies in which the significance of side-edge vortex lift in supersonic flow can be investigated.

## REFERENCES

1. Lan, C. E. and Mehrotra, S. C. "An Improved Woodward's Panel Method for Calculating Edge Suction Forces," Journal of Aircraft, Vol. 16, September 1979, pp. 632-635.
2. Lan, C. E. and Mehrotra, S. C., "An Improved Woodward's Panel Method for Calculating Leading-Edge and Side-Edge Suction Forces at Subsonic and Supersonic Speeds," NASA CR-3205, November 1979.
3. Lamar, J. E. and Gloss, B. B., "Subsonic Aerodynamic Characteristics of Interacting Lifting Surfaces with Separated Flow Around Sharp Edges Predicted by a Vortex-Lattice Method," NASA TN D-7921, September 1975.
4. Lamar, J. E., "Subsonic Vortex-Flow Design Study for Slender Wings," Journal of Aircraft, Vol. 15, September 1978, pp. 611-617.
5. Lamar, J. E., Schemensky, R. T., and Reddy, C. S., "Development of a Vortex-Lift-Design Method and Application to a Slender Maneuver-Wing Configuration," AIAA Paper 80-0327, Presented at the AIAA 18th Aerospace Sciences Meeting, Pasadena, California, January 1980.
6. Polhamus, E. C., "A Concept of the Vortex Lift of Sharp-Edge Delta Wings Based on a Leading-Edge-Suction Analogy," NASA TN D-3767, December 1966.
7. Wentz, W. H., Jr., "Effects of Leading-Edge Camber on Low-Speed Characteristics of Slender Delta Wings," NASA CR-2002, October 1972.
8. Rao, D. M., "Leading Edge Vortex-Flap Experiments on a 74 deg. Delta Wing," NASA CR-159161, November 1979.
9. Korn, G. A. and Korn, T. M., "Mathematical Handbook for Scientists and Engineers," McGraw-Hill, New York, 1961.
10. Earnshaw, P. B., "An Experimental Investigation of the Structure of a Leading-Edge Vortex," British Aeronautical Research Council, Reports and Memoranda No. 3281, March 1961.
11. Lan, C. E., "A Quasi-Vortex-Lattice Method in Thin Wing Theory," Journal of Aircraft, Vol. 11, September 1974, pp. 518-527.
12. Lan, C. E., "Calculation of Lateral-Directional Stability Derivatives for Wing-Body Combinations with and without Jet Interaction Effects," NASA CR-145251, 1977.
13. Lan, C. E. and Lamar, J. E., "On the Logarithmic-Singularity Correction in the Kernel Function Method of Subsonic Lifting-Surface Theory," NASA TN D-8513, 1977.
14. Schade, R. O., "Effect of Geometric Dihedral on the Aerodynamic Characteristics of Two Isolated Vee-Tail Surfaces," NACA TN 1369, July 1947.
15. Washburn, K. E. and Gloss, B. B., "Effect of Wing-Tip Dihedral on the Longitudinal and Lateral Aerodynamic Characteristics of a Supersonic Cruise Configuration at Subsonic Speeds," NASA TM X-72693, August 1976.

16. Brown, C. E. and Michael, W. H., Jr., "On Slender Delta Wings with Leading-Edge Separation," NACA TN 3430, April 1955.
17. Nangia, R. K. and Hancock, G. J., "A Theoretical Investigation for Delta Wings with Leading-Edge Separation at Low Speeds," Aeronautical Research Council of Great Britain, C. P. 1086, August 1968.
18. Smith, J. H. B., "Improved Calculations of Leading-Edge Separation from Slender, Thin, Delta Wings," Proceedings of Royal Society of London, Series A 306, pp. 67-90, 1968.
19. Squire, L. C., "Camber Effects on the Non-Linear Lift of Slender Wings with Sharp Leading Edges," Aeronautical Research Council of Great Britain, C. P. No. 924, January 1966.
20. Menees, G. P., "Lift, Drag, and Pitching Moment of an Aspect-Ratio-2 Triangular Wing with Leading-Edge Flaps Designed to Simulate Conical Camber," NASA Memo 10-5-58A, December 1958.
21. Mehrotra, S. C. and Lan, C. E., "A Theoretical Investigation of the Aerodynamics of Low-Aspect-Ratio Wings with Partial Leading-Edge Separation," NASA CR-145304, January 1978.
22. Polhamus, E. C., "Prediction of Vortex-Lift Characteristics by a Leading-Edge Suction Analogy," Journal of Aircraft, Vol. 8, No. 4, April 1971, pp. 193-199.
23. Igglesden, M. S., "Wind Tunnel Measurements of the Lift-Dependent drag of Thin Conically Cambered Slender Delta Wings at Mach Numbers 1.4 and 1.8," Royal Aircraft Establishment of Great Britain, Technical Note No. Aero. 2677, April 1960.
24. Carlson, H. W. and Mack, R. J., "Studies of Leading-Edge Thrust Phenomena," Journal of Aircraft, Vol. 17, December 1980, pp. 890-897.
25. Squire, L. C., Jones, J. G., and Stanbrook, A., "An Experimental Investigation of the Characteristics of Some Plane and Cambered  $65^\circ$  Delta Wings at Mach Numbers from 0.7 to 2.0," Aeronautical Research Council of Great Britain, Reports and Memoranda 3305, July 1961.
26. Lighthill, M. J., "Higher Approximations" in General Theory of High Speed Aerodynamics, Edited by W. R. Sears, Princeton University Press, 1954.
27. Hill, W. A. Jr., "Experimental Lift of Low-Aspect-Ratio Triangular Wings at Large Angles of Attack and Supersonic Speeds," NACA RM A57I17, November 1957.
28. Sorrells, R. B. III and Landrum, E. J., "Theoretical and Experimental Study of Twisted and Cambered Delta Wings Designed for a Mach Number of 3.5," NASA TN D-8247, August 1976.
29. Middleton, W. D. and Carlson, H. W., "Numerical Method of Estimating and Optimizing Supersonic Aerodynamic Characteristics of Arbitrary Planform Wings," Journal of Aircraft, Vol. 2, July-August 1965, pp. 261-265.
30. Dollyhigh, S. M., "Theoretical Evaluation of High-Speed Aerodynamics for Arrow-Wing Configurations," NASA TP-1358, 1979.

# APPENDIX A

## Derivation of Expressions for Camber Slopes, $\frac{\partial z_c}{\partial x}$ and $\frac{\partial z_c}{\partial y}$

As indicated in Section 3, the camber slopes,  $\frac{\partial z_c}{\partial x}$  and  $\frac{\partial z_c}{\partial y}$ , based on the original XYZ system (see fig. 1) can be expressed in terms of camber slopes based on the local chord line. To achieve this, two rotations of the coordinate system are needed. The first is about the original X-axis through a dihedral angle ( $\phi$ ), and the second is about the new Y-axis ( $Y_1$ -axis) through a local twist angle ( $\alpha_{tw}$ ). The resulting expressions for  $\frac{\partial z_c}{\partial x}$  and  $\frac{\partial z_c}{\partial y}$  are derived below.

### A.1 Calculation of $\frac{\partial z_c}{\partial x}$

Consider a vector with components ( $dx, dy, dz_c$ ) tangent to the camber surface at some point, P. This vector has the component  $\vec{PQ}$  in the X-Z plane (fig. 2). According to vector analysis, the vector ( $dx, dy, dz_c$ ) based on the XYZ system can be expressed in the  $X'_2Y'_2Z'_2$  system ( $dx_2, dy_2, d\bar{z}_c$ ) through the following relation (p. 413, reference 9):

$$\begin{pmatrix} dx_2 \\ dy_2 \\ d\bar{z}_c \end{pmatrix} = \begin{bmatrix} \cos \alpha_{tw} & 0 & -\sin \alpha_{tw} \\ 0 & 1 & 0 \\ \sin \alpha_{tw} & 0 & \cos \alpha_{tw} \end{bmatrix} \begin{bmatrix} 1 & 0 & 0 \\ 0 & \cos \phi & \sin \phi \\ 0 & -\sin \phi & \cos \phi \end{bmatrix} \begin{pmatrix} dx \\ dy \\ dz_c \end{pmatrix}$$

$$= \begin{bmatrix} \cos \alpha_{tw} & \sin \alpha_{tw} \sin \phi & -\sin \alpha_{tw} \cos \phi \\ 0 & \cos \phi & \sin \phi \\ \sin \alpha_{tw} & -\sin \phi \cos \alpha_{tw} & \cos \phi \cos \alpha_{tw} \end{bmatrix} \begin{pmatrix} dx \\ dy \\ dz_c \end{pmatrix} \quad (A.1)$$

It follows from equation (A.1) that

$$dx_2 = dx \cos \alpha_{tw} + dy \sin \alpha_{tw} \sin \phi - dz_c \sin \alpha_{tw} \cos \phi \quad (A.2)$$

$$dy_2 = dy \cos \phi + dz_c \sin \phi \quad (A.3)$$

$$d\bar{z}_c = dx \sin \alpha_{tw} - dy \sin \phi \cos \alpha_{tw} + dz_c \cos \phi \cos \alpha_{tw} \quad (A.4)$$



To calculate  $\frac{\partial z_c}{\partial x}$  in terms of  $\frac{d\bar{z}_c}{dx_2} \Big|_{y=\text{constant}}$ , set  $dy = 0$  in equations (A.2)-(A.4). Hence,

$$dx_2 = dx \cos \alpha_{tw} - dz_c \sin \alpha_{tw} \cos \phi \quad (A.5)$$

$$d\bar{z}_c = dx \sin \alpha_{tw} + dz_c \cos \phi \cos \alpha_{tw} \quad (A.6)$$

Equations (A.5) and (A.6) can be solved for  $dx$  and  $dz_c$  through Cramer's rule to give:

$$dz_c = \frac{-dx_2 \sin \alpha_{tw} + d\bar{z}_c \cos \alpha_{tw}}{\cos \phi} \quad (A.7)$$

$$dx = dx_2 \cos \alpha_{tw} + d\bar{z}_c \sin \alpha_{tw} \quad (A.8)$$

To find  $\frac{\partial z_c}{\partial x}$ , equation (A.7) is divided through by equation (A.8) to yield:

$$\frac{\partial z_c}{\partial x} = \frac{-\sin \alpha_{tw} + \frac{d\bar{z}_c}{dx_2} \cos \alpha_{tw}}{\cos \phi (\cos \alpha_{tw} + \frac{d\bar{z}_c}{dx_2} \sin \alpha_{tw})} \quad (A.9)$$

or,

$$\cos \phi \frac{\partial z_c}{\partial x} = \frac{-\sin \alpha_{tw} + \frac{d\bar{z}_c}{dx_2} \cos \alpha_{tw}}{\cos \alpha_{tw} + \frac{d\bar{z}_c}{dx_2} \sin \alpha_{tw}} \quad (A.10)$$

For  $\phi = 0$ , let  $\frac{\partial z_c}{\partial x} = \tan \theta$  and  $\frac{d\bar{z}_c}{dx_2} = \tan \delta_c$ . Both  $\theta$  and  $\delta_c$  are indicated in figure 2. Equation (A.10) then becomes

$$\begin{aligned} \tan \theta &= \frac{-\sin \alpha_{tw} \cos \delta_c + \sin \delta_c \cos \alpha_{tw}}{\cos \alpha_{tw} \cos \delta_c + \sin \delta_c \sin \alpha_{tw}} = \frac{\sin (\delta_c - \alpha_{tw})}{\cos (\delta_c - \alpha_{tw})} \\ &= \tan (\delta_c - \alpha_{tw}) \end{aligned}$$

Hence,

$$\theta = \delta_c - \alpha_{tw} \quad (A.11)$$

The result in equation (A.11) is seen to be correct from a geometric point of view, because in figure 2,  $\theta$  is negative and  $\delta_c$  is positive.

A.2 Calculation of  $\frac{\partial z_c}{\partial y}$

To calculate  $\frac{\partial z_c}{\partial y}$  in terms of  $\frac{d\bar{z}_c}{dy_2}$ , set  $dx = 0$  in equations (A.2)-(A.4).

It follows that:

$$dy_2 = dy \cos \phi + dz_c \sin \phi \quad (A.12)$$

$$d\bar{z}_c = -dy \sin \phi \cos \alpha_{tw} + dz_c \cos \phi \cos \alpha_{tw} \quad (A.13)$$

Solving equations (A.12) and (A.13) for  $dz_c$  and  $dy$  through Cramer's rule,

it is obtained that

$$dz_c = \frac{dy_2 \sin \phi \cos \alpha_{tw} + d\bar{z}_c \cos \phi}{\cos \alpha_{tw}}$$

$$dy = \frac{dy_2 \cos \phi \cos \alpha_{tw} - d\bar{z}_c \sin \phi}{\cos \alpha_{tw}}$$

Hence,

$$\frac{\partial z_c}{\partial y} = \frac{\sin \phi \cos \alpha_{tw} + \frac{d\bar{z}_c}{dy_2} \cos \phi}{\cos \phi \cos \alpha_{tw} - \frac{d\bar{z}_c}{dy_2} \sin \phi} \quad (A.14)$$

## APPENDIX B

### Geometry of Leading-Edge Plane Flaps and Conical Camber

In this report, leading-edge plane flaps and conical camber have been used extensively to demonstrate the applications of the present program. These two kinds of aerodynamic devices have been represented analytically in the program. For the convenience of readers, these analytical expressions are developed in the following.

#### B.1. Leading-Edge Plane Flaps

A leading-edge plane flap, as shown in figure B.1, is defined by four corner points, 1-2-3-4. In applications, points 1 and 2, or points 3 and 4, may coincide. Therefore, to define a normal vector to the plane, it is convenient to use the two vectors  $\vec{T}_1$  and  $\vec{T}_2$  given by:

$$\vec{T}_1 = (x_4 - x_1)\vec{i} + (y_4 - y_1)\vec{j} + (z_4 - z_1)\vec{k} \quad (B.1)$$

$$\vec{T}_2 = (x_3 - x_2)\vec{i} + (y_3 - y_2)\vec{j} + (z_3 - z_2)\vec{k} \quad (B.2)$$

A normal vector ( $\vec{N}$ ) to the plane flap can now be constructed by using  $\vec{T}_1$  and  $\vec{T}_2$ :

$$\begin{aligned} \vec{N} = \vec{T}_1 \times \vec{T}_2 &= \begin{vmatrix} \vec{i} & \vec{j} & \vec{k} \\ x_4 - x_1 & y_4 - y_1 & z_4 - z_1 \\ x_3 - x_2 & y_3 - y_2 & z_3 - z_2 \end{vmatrix} \\ &= \vec{i} [(y_4 - y_1)(z_3 - z_2) - (y_3 - y_2)(z_4 - z_1)] \\ &\quad + \vec{j} [(x_3 - x_2)(z_4 - z_1) - (x_4 - x_1)(z_3 - z_2)] \\ &\quad + \vec{k} [(x_4 - x_1)(y_3 - y_2) - (x_3 - x_2)(y_4 - y_1)] \\ &= N_x \vec{i} + N_y \vec{j} + N_z \vec{k} \end{aligned} \quad (B.3)$$

It follows that if the equation of a plane containing the flap is written as

$$ax + by + cz + d = 0 \quad (B.4)$$

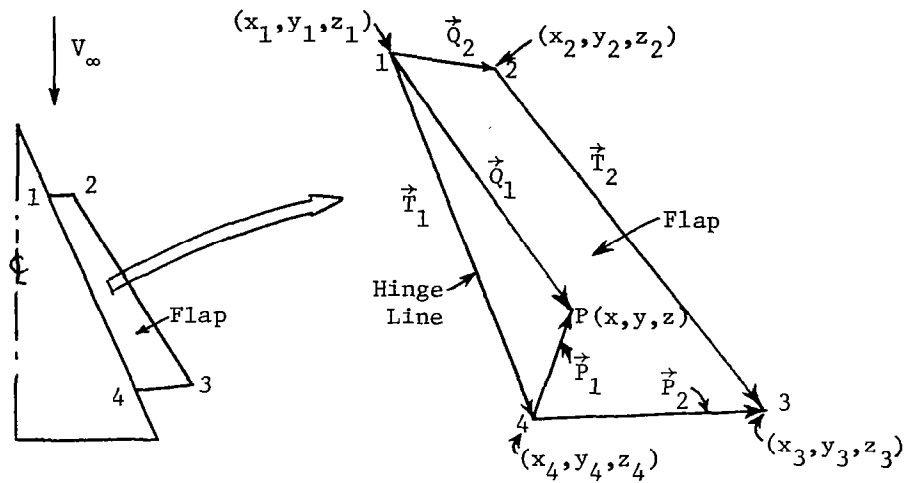


Figure B. 1 Geometry of a Leading-Edge Plane Flap

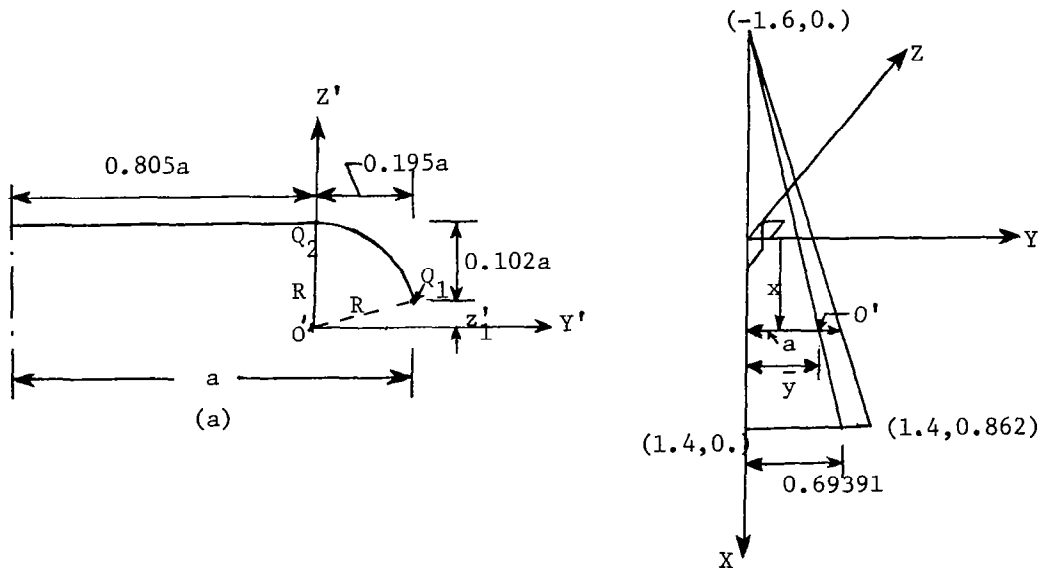


Figure B. 2 Geometry of a Delta Wing with Conical Camber

the constants, a, b, and c can be chosen as follows:

$$a = N_x, \quad b = N_y, \quad c = N_z \quad (\text{B.5})$$

The camber slopes,  $\frac{\partial \bar{z}_c}{\partial x}$  and  $\frac{\partial \bar{z}_c}{\partial y}$ , needed in determining the aerodynamic characteristics can then be obtained by differentiating equation (B.4) after  $z$  is replaced by  $\bar{z}_c$ :

$$\frac{\partial \bar{z}_c}{\partial x} = -\frac{a}{c} = -\frac{N_x}{N_z} \quad (\text{B.6})$$

$$\frac{\partial \bar{z}_c}{\partial y} = -\frac{b}{c} = -\frac{N_y}{N_z} \quad (\text{B.7})$$

To determine whether a point  $P(x, y, z)$  (such as a control point) is within the boundary of the plane formed by the points 1-2-3-4, the two vectors  $\vec{Q}_1$  and  $\vec{Q}_2$  formed by points 1-P and 1-2, respectively, can be used. When projected onto the X-Y plane, these two vectors will be denoted by  $\vec{Q}'_1$  and  $\vec{Q}'_2$ . It follows that

$$\begin{aligned} \vec{Q}'_1 \times \vec{Q}'_2 &= \begin{vmatrix} \vec{i} & \vec{j} & \vec{k} \\ x - x_1 & y - y_1 & 0 \\ x_2 - x_1 & y_2 - y & 0 \end{vmatrix} \\ &= \vec{k} [(x - x_1)(y_2 - y_1) - (x_2 - x_1)(y - y_1)] \end{aligned} \quad (\text{B.8})$$

It follows that if  $\vec{Q}'_1 \times \vec{Q}'_2 > 0$ , the point P is on the flap-side of the line connecting points 1 and 2. In case  $\vec{Q}'_2$  is a zero vector (i.e., points 1 and 2 coincide), comparison of y-coordinates of points 1 and P will be sufficient to determine whether P is inboard or outboard of point 1. Similarly, the two vectors  $\vec{P}'_1$  and  $\vec{P}'_2$  formed by points 4-P and 4-3, respectively, and projected onto the X-Y plane can be used to determine the location of P relative to the boundary of the line 4-3:

$$\vec{P}_1' \times \vec{P}_2' = \begin{vmatrix} \vec{i} & \vec{j} & \vec{k} \\ x - x_4 & y - y_4 & 0 \\ x_3 - x_4 & y_3 - y_4 & 0 \end{vmatrix}$$

$$= \vec{k}[(x - x_4)(y_3 - y_4) - (x_3 - x_4)(y - y_4)] \quad (B.9)$$

If  $\vec{P}_1' \times \vec{P}_2' < 0$ , the point P is again on the flap-side of the line connecting points 4 and 3. Again, if points 4 and 3 coincide, the y-coordinates of point P and 4 may be compared to determine the location of P relative point 4.

## B.2 Conical Camber

Leading-edge plane flaps, described in Section B.1, are simple devices frequently used to simulate aerodynamically the effect of more complicated camber shapes, such as conical camber. However, many test models have been incorporated with leading-edge conical camber of different sizes. To illustrate the derivation of analytical expressions describing the geometry of such conical cambers, the one used in reference 7 on a delta wing will be used as an example.

As shown in figure B.2,  $Q_1Q_2$  is a circular arc with circle center at  $O'$ . Since the point  $Q_1$  is on the circular arc, it follows that (see fig. B.2(a))

$$(0.195a)^2 + z_1'^2 = R^2 \quad (B.10)$$

$$0.102a + z_1' = R \quad (B.11)$$

Substituting equation (B.11) into equation (B.10) results in

$$(0.195a)^2 + (R - 0.102a)^2 = R^2$$

which can be solved for R:

$$R = 0.237397 a \quad (B.12)$$

Based on the planform coordinate system as shown in figure B.2(b), the center of circle  $O'$  is at  $(x, \bar{y}, -R)$ , where

$$\bar{y} = 0.231303 (1.6+x) \quad (B.13)$$

$$\begin{aligned} R &= 0.237397 a = 0.237397 \times \frac{0.862}{3.0} (1.6+x) \\ &= 0.06821207 (1.6+x) \end{aligned} \quad (B.14)$$

Hence, the equation of circular arc based on the planform coordinate system becomes

$$(y - \bar{y})^2 + (z + R)^2 = R^2, \quad y \geq \bar{y}, \quad z < 0 \quad (B.15)$$

To find  $\frac{\partial \bar{z}_c}{\partial x}$ , replace  $z$  in equation (B.15) by  $\bar{z}_c$  and differentiate the equation with respect to  $x$ . It is obtained that

$$2(y - \bar{y}) \left(-\frac{\partial \bar{y}}{\partial x}\right) + 2(\bar{z}_c + R) \left(\frac{\partial \bar{z}_c}{\partial x} + \frac{\partial R}{\partial x}\right) = 2R \frac{\partial R}{\partial x}$$

but

$$\frac{\partial \bar{y}}{\partial x} = 0.231303$$

$$\frac{\partial R}{\partial x} = 0.06821207$$

Hence,

$$\frac{\partial \bar{z}_c}{\partial x} = \frac{1}{\bar{z}_c + R} \left[ 0.231303 (y - \bar{y}) - 0.068212 (\bar{z}_c) \right], \quad y \geq \bar{y} \quad (B.16)$$

where  $\bar{z}_c$  is given by

$$\bar{z}_c = -R + \sqrt{R^2 - (y - \bar{y})^2}, \quad y \geq \bar{y} \quad (B.17)$$

To find  $\frac{\partial \bar{z}_c}{\partial y}$ , equation (B.15) is differentiated with respect to  $y$ :

$$\frac{\partial \bar{z}_c}{\partial y} = -\frac{y - \bar{y}}{\bar{z}_c + R}, \quad y \geq \bar{y} \quad (B.18)$$

## APPENDIX C

### A Numerical Method for Calculating $\frac{\partial \bar{z}_c}{\partial y}$

When a general camber surface is described by a finite number of ordinates at some spanwise stations, a numerical method is needed to calculate  $\frac{\partial \bar{z}_c}{\partial x}$  and  $\frac{\partial \bar{z}_c}{\partial y}$  at control points and integration (pressure) points. In the present program,  $\frac{\partial \bar{z}_c}{\partial x}$  is calculated through cubic spline interpolation. In the following, a trigonometric interpolation formula will be used to calculate  $\frac{\partial \bar{z}_c}{\partial y}$ . The method used is similar to that used in determining the distribution of streamwise vortex density (ref. 12).

It is well-known that if at a given point, slopes in two directions are known, then the slope in other directions can be determined in terms of them. Referring to figure C.1, assume that the slopes in the X- and Y'-directions are known. To calculate the slope in the y-direction, the following coordinate transformation formulas are needed.

$$x' = x \cos \Lambda - y \sin \Lambda \quad (C.1)$$

$$y' = x \sin \Lambda + y \cos \Lambda \quad (C.2)$$

If  $z_c(x, y)$  is the dimensional camber function, then

$$\frac{\partial z_c}{\partial y} = \frac{\partial z_c}{\partial x'} \frac{\partial x'}{\partial y} + \frac{\partial z_c}{\partial y'} \frac{\partial y'}{\partial y} = -\sin \Lambda \frac{\partial z_c}{\partial x'} + \cos \Lambda \frac{\partial z_c}{\partial y'} \quad (C.3)$$

$$\frac{\partial z_c}{\partial x} = \frac{\partial z_c}{\partial x'} \frac{\partial x'}{\partial x} + \frac{\partial z_c}{\partial y'} \frac{\partial y'}{\partial x} = \cos \Lambda \frac{\partial z_c}{\partial x'} + \sin \Lambda \frac{\partial z_c}{\partial y'} \quad (C.4)$$

Substituting  $\frac{\partial z_c}{\partial x}$  obtained from equation (C.4) into equation (C.3) results in:

$$\frac{\partial z_c}{\partial y} = -\tan \Lambda \frac{\partial z_c}{\partial x} + \frac{1}{\cos \Lambda} \frac{\partial z_c}{\partial y'} \quad (C.5)$$

Equation (C.5) represents the basic formula used in the present method. To determine  $\frac{\partial z_c}{\partial y'}$ ,  $z_c$ -ordinates in the y'-direction are used. Although cubic spline interpolation can be used to find  $\frac{\partial z_c}{\partial y'}$  it was found to be more accurate to use the trigonometric interpolation formula (ref. 12):



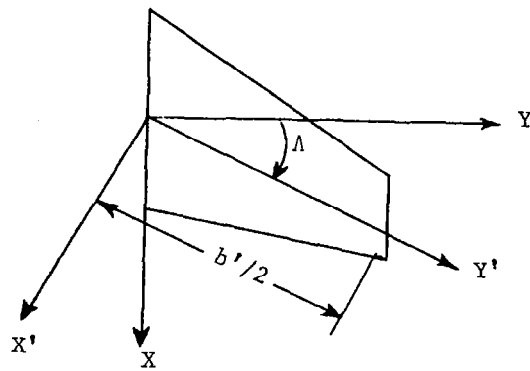


Figure C. 1 Coordinate Transformation.

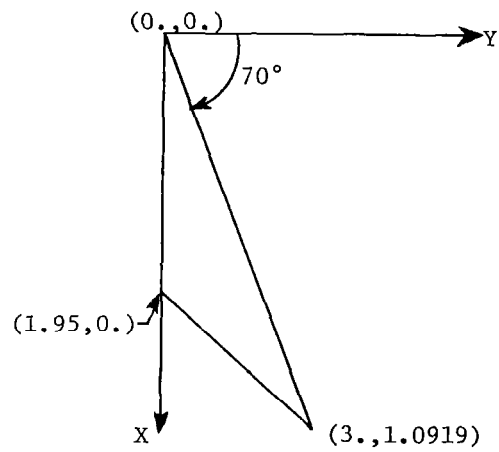


Figure C. 2 Arrow Wing used in the Example.

$$\frac{\partial z_c}{\partial y'_i} = \frac{dz_c}{d\theta_i} \frac{2}{b' \sin \theta_i} \quad (C.6)$$

$$\begin{aligned} \frac{dz_c}{d\theta_i} = & \sum_{k=1}^{M-1}, z_{c_k} (-1)^{k+i} \frac{\sin \theta_i}{\cos \theta_k - \cos \theta_i} + \frac{1}{2} z_{c_i} \frac{\cos \theta_i}{\sin \theta_i} \\ & + \frac{1}{2} z_{c_o} \frac{(-1)^i \sin \theta_i}{1 - \cos \theta_i} - \frac{1}{2} z_{c_M} (-1)^{M+i} \frac{\sin \theta_i}{1 + \cos \theta_i} \end{aligned} \quad (C.7)$$

where:

$$y' = \frac{b'}{2} (1 - \cos \theta) \quad (C.8)$$

$$\theta_i = \frac{i\pi}{M}, \quad \theta_k = \frac{k\pi}{M} \quad (C.9)$$

$$i = 1, \dots, M-1.$$

where the prime on the summation sign implies that the term with  $k = i$  is to be omitted. In equation (C.7),  $z_{c_o}$  and  $z_{c_M}$  are the camber ordinates at inboard and outboard endpoints, respectively, and  $M$  is the total number of points used in the interpolation.

To indicate the accuracy of the interpolation method, an arrow wing with the following camber surface is chosen (See figure C.2):

$$\begin{aligned} \bar{z}_c(\bar{x}, \bar{y}) = & (0.14 - 0.22\bar{y})\bar{x}^3 + (-0.1835 + 0.165\bar{y})\bar{x}^2 + 0.0785\bar{x} \\ & + 0.015(\bar{y} - 1.0) \end{aligned} \quad (C.10)$$

$$\bar{y} = y/b/2, \quad \bar{x} = (x - x_{le}(\bar{y}))/c(\bar{y}), \quad \bar{z}_c = z_c/c(\bar{y}) \quad (C.11)$$

It follows that

$$\begin{aligned} \frac{\partial z_c}{\partial y} &= \frac{\partial z_c}{\partial \bar{y}} \frac{\partial \bar{y}}{\partial y} \\ &= \frac{\partial \bar{y}}{\partial y} \left[ c(\bar{y}) \frac{\partial \bar{z}_c(\bar{y})}{\partial \bar{y}} + \bar{z}_c(\bar{y}) \frac{\partial c(\bar{y})}{\partial \bar{y}} \right] \end{aligned} \quad (C.12)$$

For the configuration shown in figure C.2,

$$\bar{x} = (x - y \tan \Lambda_{le}) / c(\bar{y}) = \frac{x - 3\bar{y}}{c_r (1 - \bar{y})} \quad (C.13)$$

where:

$$c(\bar{y}) = c_r (1 - \bar{y}) \quad (C.14)$$

$$\frac{\partial c(\bar{y})}{\partial \bar{y}} = -c_r = -1.95 \quad (C.15)$$

From equation (C.10),

$$\begin{aligned} \frac{\partial \bar{z}_c}{\partial \bar{y}} = & -0.22 \bar{x}^3 + 0.165 \bar{x}^2 + 0.015 + [(0.42 - 0.66\bar{y}) \bar{x}^2 \\ & + (-0.367 + 0.33\bar{y}) \bar{x} + 0.0785] \frac{\partial \bar{x}}{\partial \bar{y}} \end{aligned} \quad (C.16)$$

Using equation (C.13), the derivative  $\frac{\partial \bar{x}}{\partial \bar{y}}$  can be obtained:

$$\frac{\partial \bar{x}}{\partial \bar{y}} = \frac{x - 3}{c_r (1 - \bar{y})^2} \quad (C.17)$$

Substituting equations (C.14)-(C.17) into (C.12) results in

$$\frac{\partial z_c}{\partial y} = \frac{2}{b} \left[ 1.95 (1 - \bar{y}) \frac{\partial \bar{z}_c}{\partial \bar{y}} - 1.95 \bar{z}_c(\bar{y}) \right] \quad (C.18)$$

with

$$\begin{aligned} \frac{\partial \bar{z}_c}{\partial \bar{y}} = & -0.22 \bar{x}^3 + 0.165 \bar{x}^2 + 0.015 + \frac{(x - 3) (0.42 - 0.66\bar{y})}{1.95 (1 - \bar{y})^2} \bar{x}^2 \\ & + \frac{(x - 3) (-0.367 + 0.33\bar{y})}{1.95 (1 - \bar{y})^2} \bar{x} + 0.0785 \frac{x - 3}{1.95 (1 - \bar{y})^2} \end{aligned} \quad (C.19)$$

Equations (C.10), (C.18) and (C.19) describe the exact distribution of  $\frac{\partial z_c}{\partial y}$  for the assumed arrow wing geometry.

Numerical results at three spanwise stations are compared with exact values in table C.1. The results along the leading edge are compared in table C.2. From both tables, it can be seen that the present numerical method is quite accurate.

Table C.1 Comparison of Calculated  $\frac{\partial z_c}{\partial y}$  with Exact Results  
at Three Spanwise Stations

$\bar{y}$	x	$\bar{x}$	$\frac{\partial z_c}{\partial y}$ Calculated	Exact
.172570	.588089	.043620	-.135850	-.135850
	.783837	.164940	-.054444	-.054436
	1.092941	.356414	.023043	.023043
	1.448850	.577098	.036728	.367278
	1.781067	.782997	-.021320	-.021320
	2.023794	.933434	-.105749	-.105749
	2.128961	.998613	-.153111	-.153111
.571157	1.749949	.043620	-.171606	-.171606
	1.851402	.164940	-.116446	-.116445
	2.011605	.356414	-.042382	-.042382
	2.196066	.577098	.017433	.017433
	2.368248	.782997	.042307	.042307
	2.494050	.933434	.037956	.037955
	2.548556	.998613	.029470	.029470
.979746	2.940962	.043620	-.208260	-.208256
	2.945754	.164940	-.180003	-.179998
	2.953320	.356414	-.109448	-.109446
	2.962032	.577098	-.002346	-.002347
	2.970163	.782997	.107531	.107529
	2.976105	.933434	.185266	.185260
	2.978679	.998613	.216633	.216628

Table C.2 Comparison of Calculated  $\frac{\partial z_c}{\partial y}$  with Exact Results  
Along the Leading Edge  $\bar{x}=0$

y	$\bar{y}$	x	$\frac{\partial z_c}{\partial y}$	
			Calculated	Exact
.022115	.020254	.060761	-.163188	-.163188
.086668	.079373	.238120	-.166355	-.166355
.188429	.172570	.517709	-.171348	-.171349
.319154	.292292	.876877	-.177763	-.177764
.468253	.428843	1.286528	-.185079	-.185080
.623647	.571157	1.713472	-.192703	-.192706
.772746	.707708	2.123122	-.200019	-.200024
.903471	.827430	2.482291	-.206433	-.206444
1.005253	.920627	2.761880	-.211427	-.211452
1.069785	.979746	2.939239	-.214594	-.214698

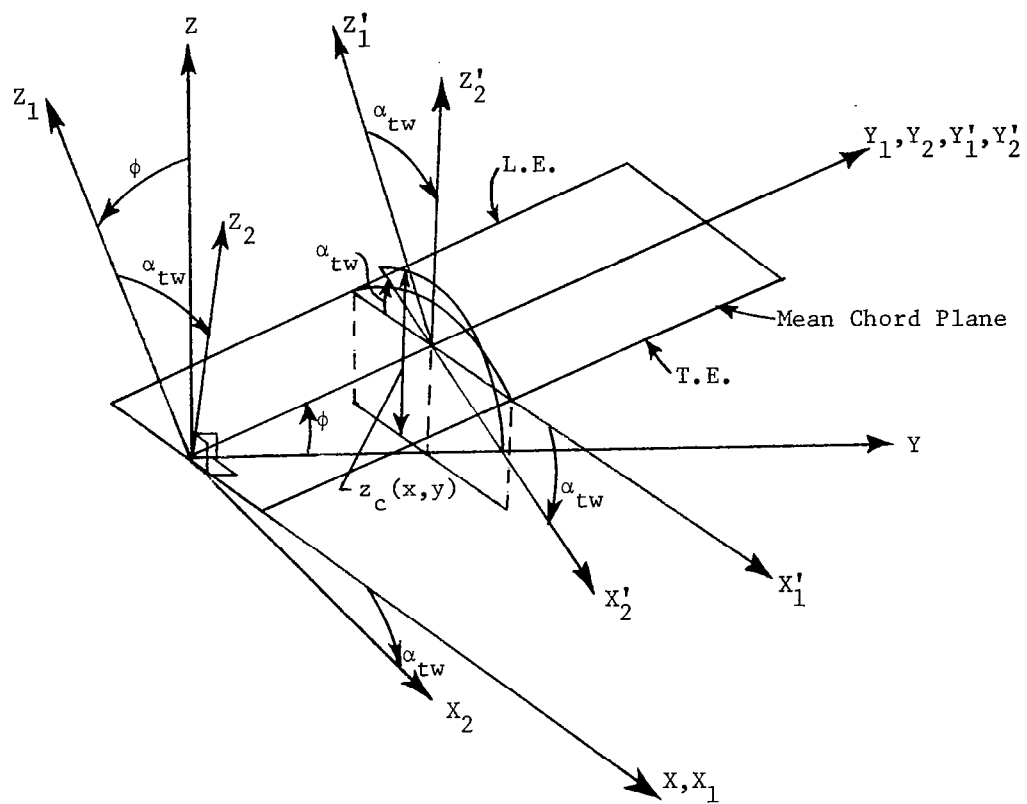


Figure 1 Definition of Variables Defining a Nonplanar Wing Surface.

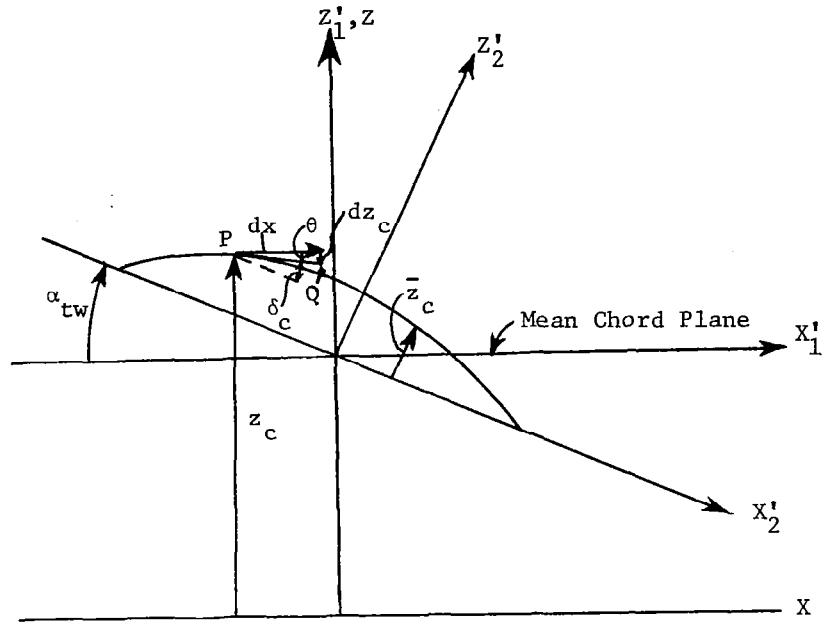


Figure 2 A Tangent Vector to the Camber Surface Being Projected to the X-Z Plane.

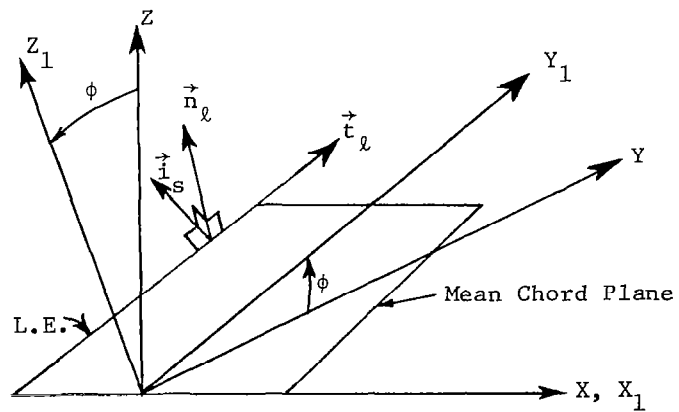


Figure 3 Unit Vectors Defined at the Leading Edge.

○ Measured Minimum Pressure Points(ref.7)

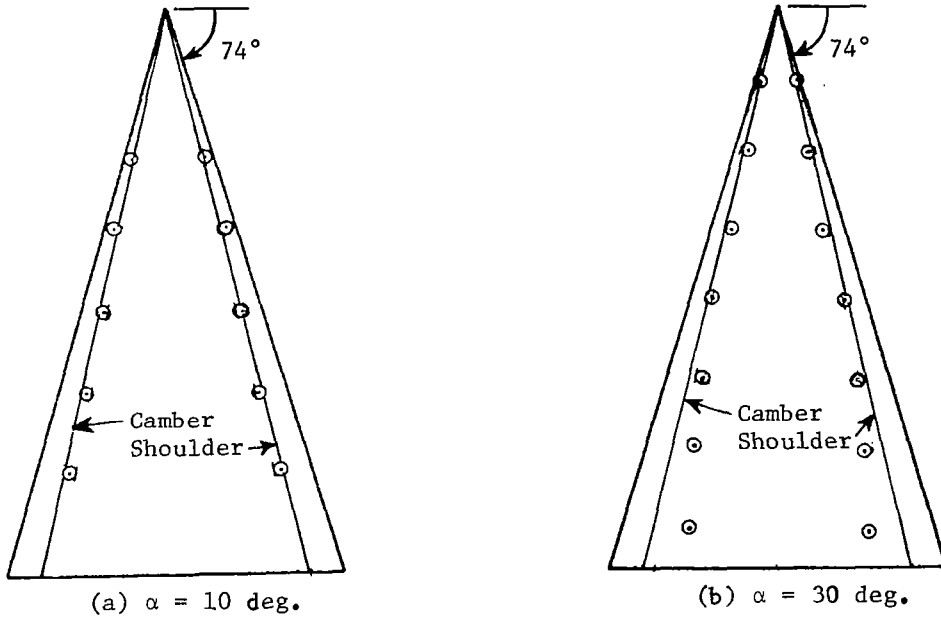


Figure 4 Measured Minimum Pressure Points as a Function of Angle of Attack on A=1.147 Delta Wing with Conical Camber.

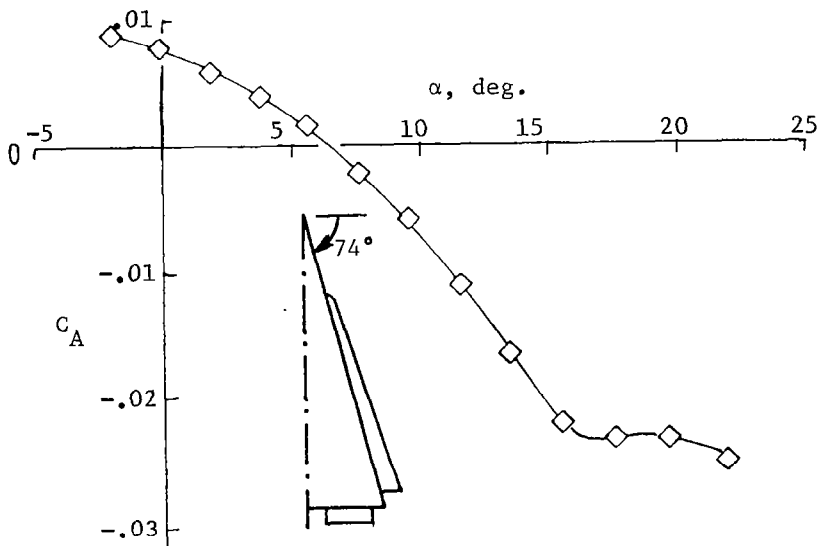


Figure 5 Axial Force Coefficient of A=1.147 Delta Wing with Vortex Flap (ref. 8).



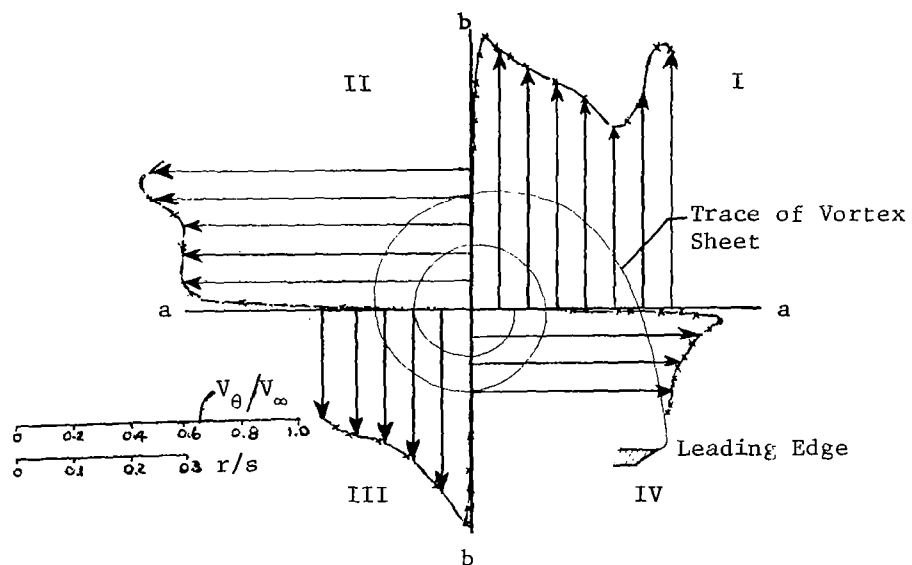
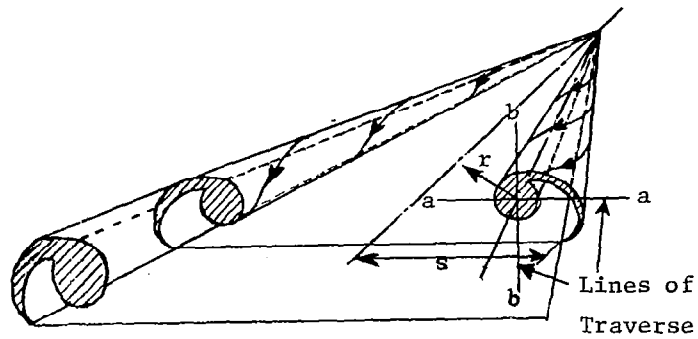


Figure 6 Measured Variation of Circumferential Velocity in Four Quadrants (ref. 10) at Angle of Attack of 14.9 deg. for  $A=1.0$  Delta Wing.

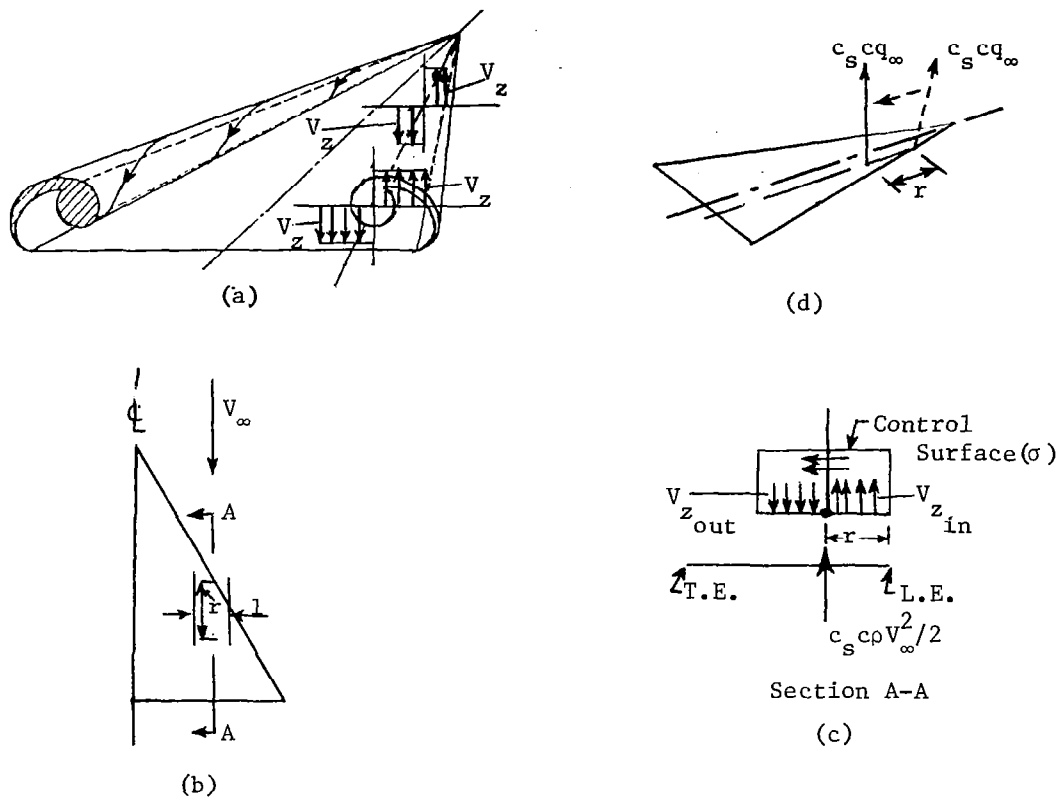


Figure 7 Geometry and Flow Field for Defining Vortex Center Location.

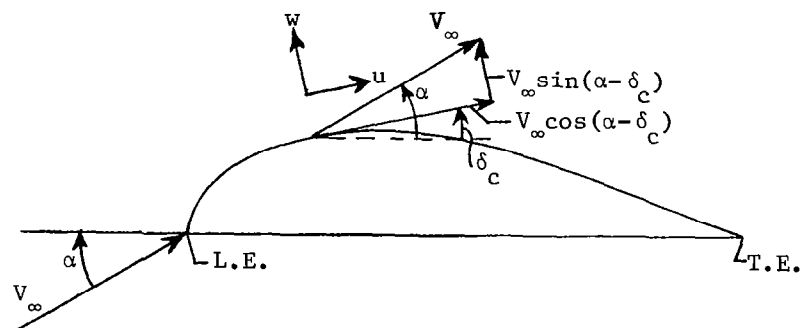


Figure 8 Velocity Components along the Camber Surface with  $\alpha_{tw} = 0$ .

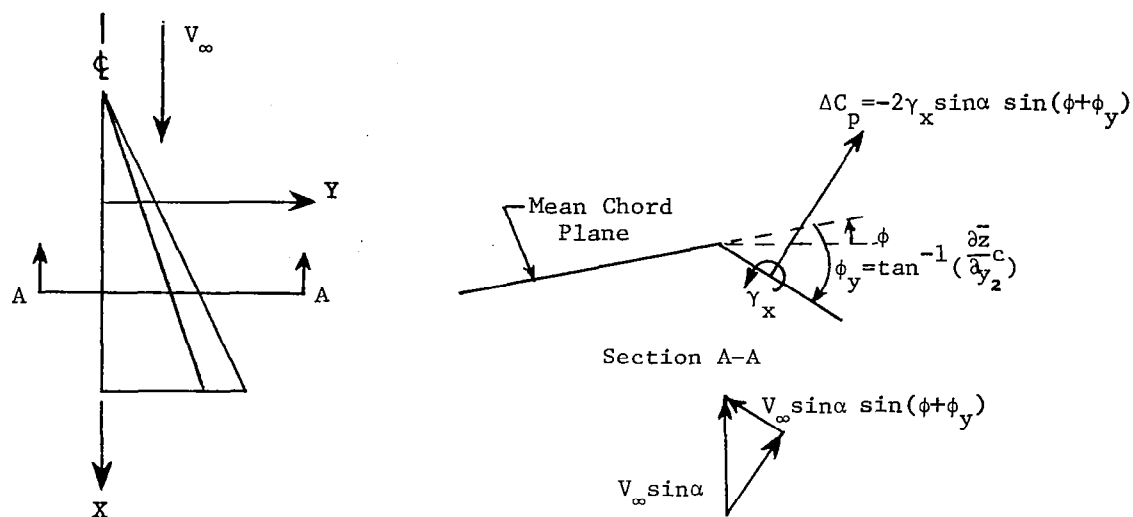


Figure 9 Geometry Showing Effect of Local Dihedral on Lifting Pressure.

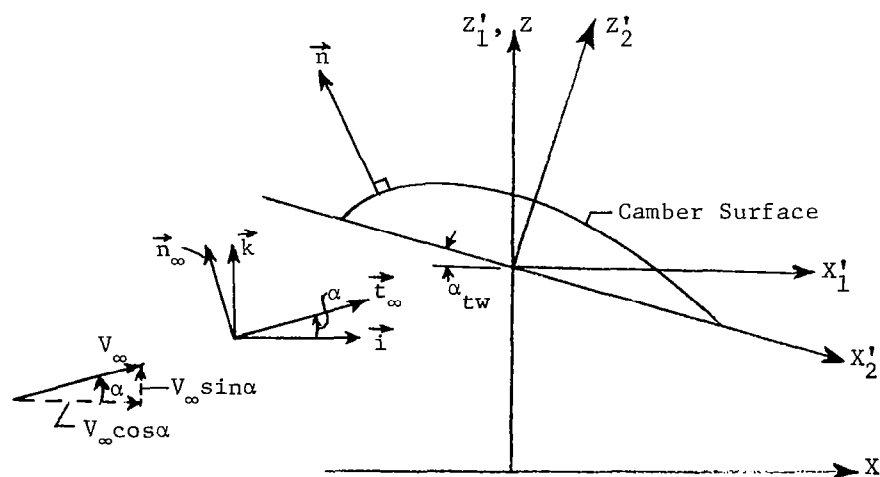
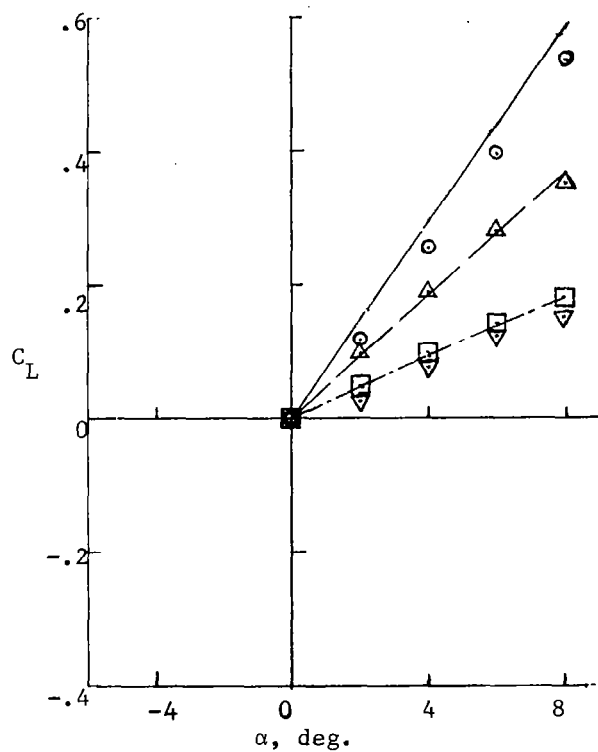
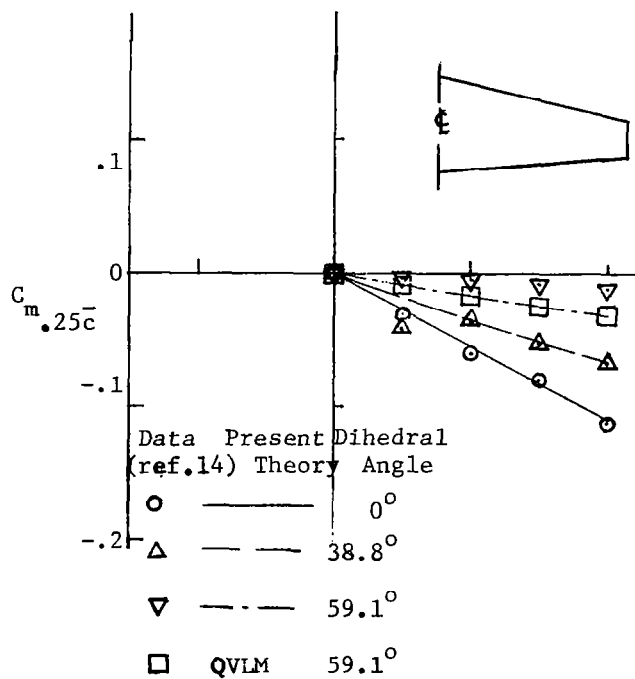
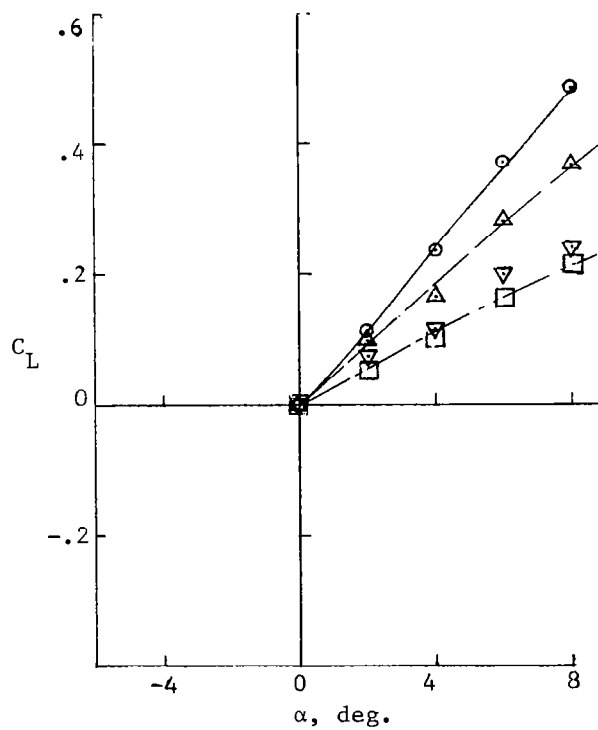
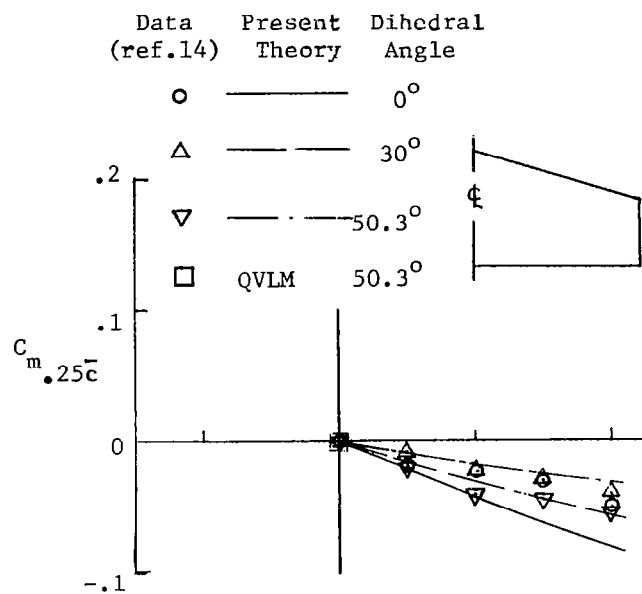


Figure 10 Geometry Defining Some Unit Vectors.



(a) Tail A.

Figure 11 Effect of Dihedral on the Aerodynamic Characteristics of V-tails at  $M=0$ .



(b) Tail B.

Figure 11 Concluded.

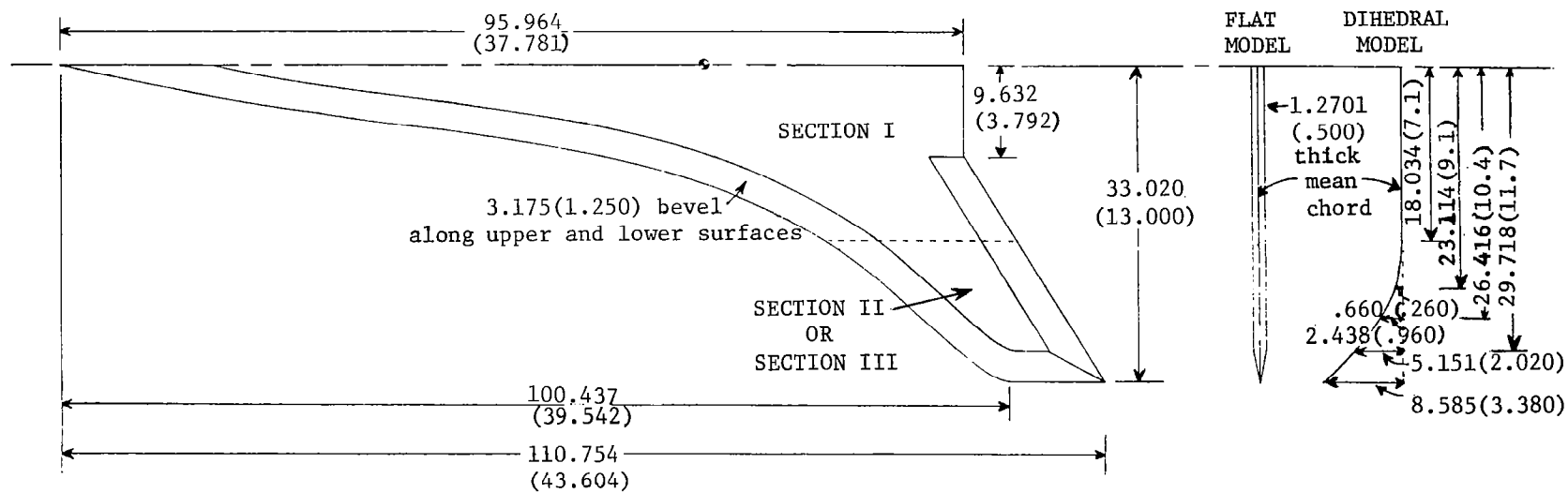


Figure 12 Geometry for a Supersonic Cruise Configuration Defined in Reference 15.  
Dimensions in cm. (in.)

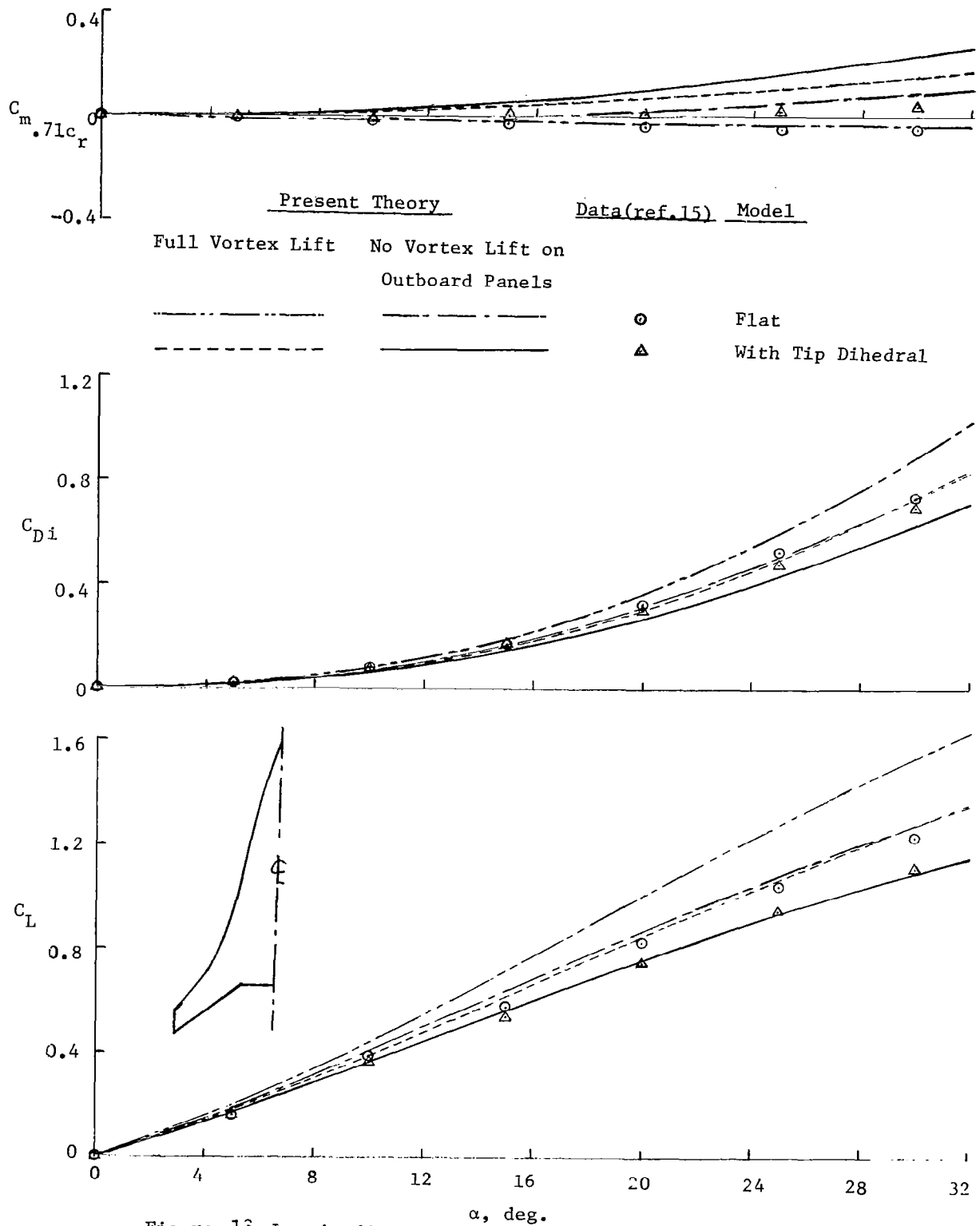


Figure 13 Longitudinal Aerodynamic Characteristics of a Supersonic Configuration at  $M=0.165$ .

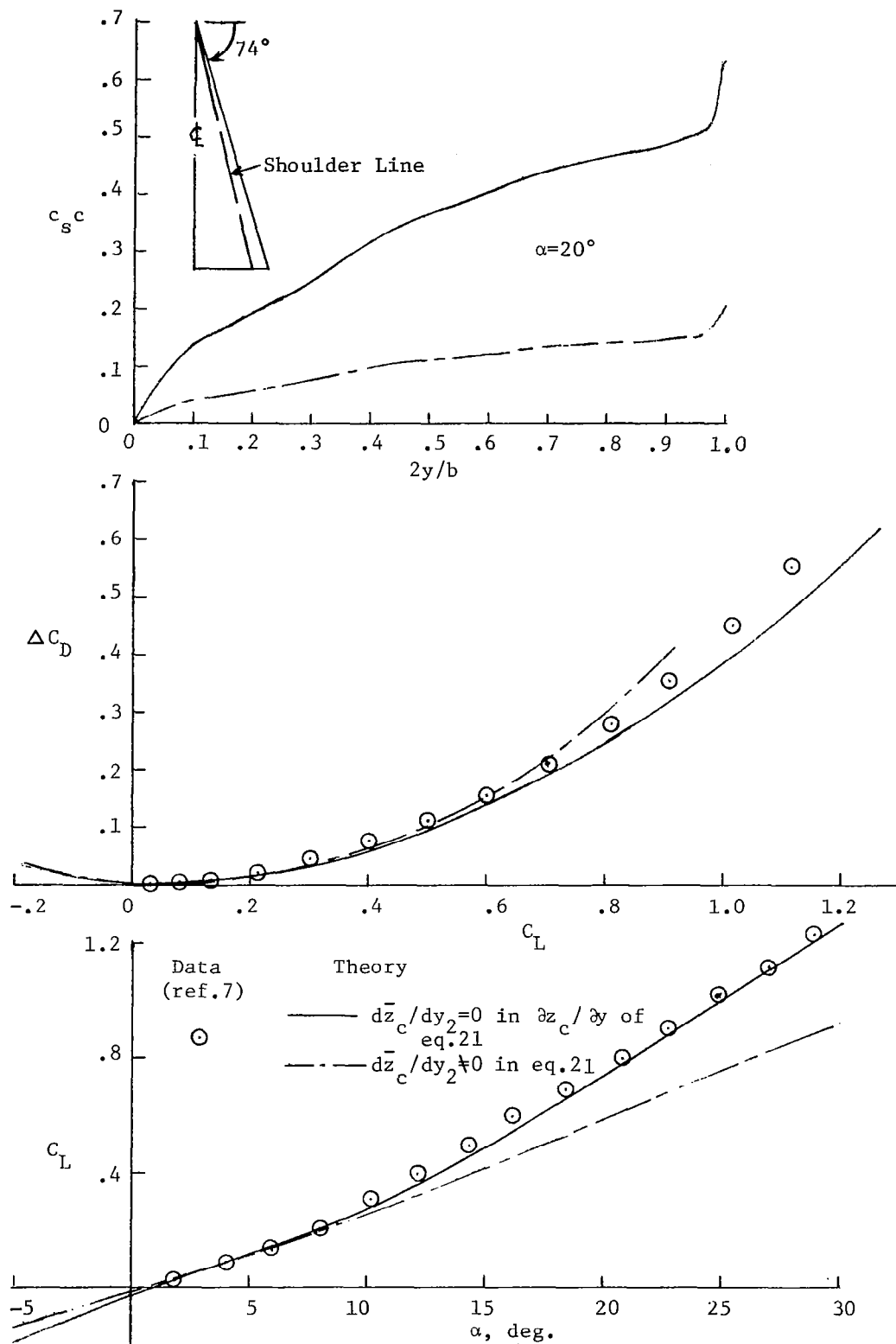


Figure 14 Effect of  $\frac{dz_c}{dy_2}$  on the Predicted Aerodynamic Characteristics of A=1.147 Delta Wing with Conical Camber at M=0.



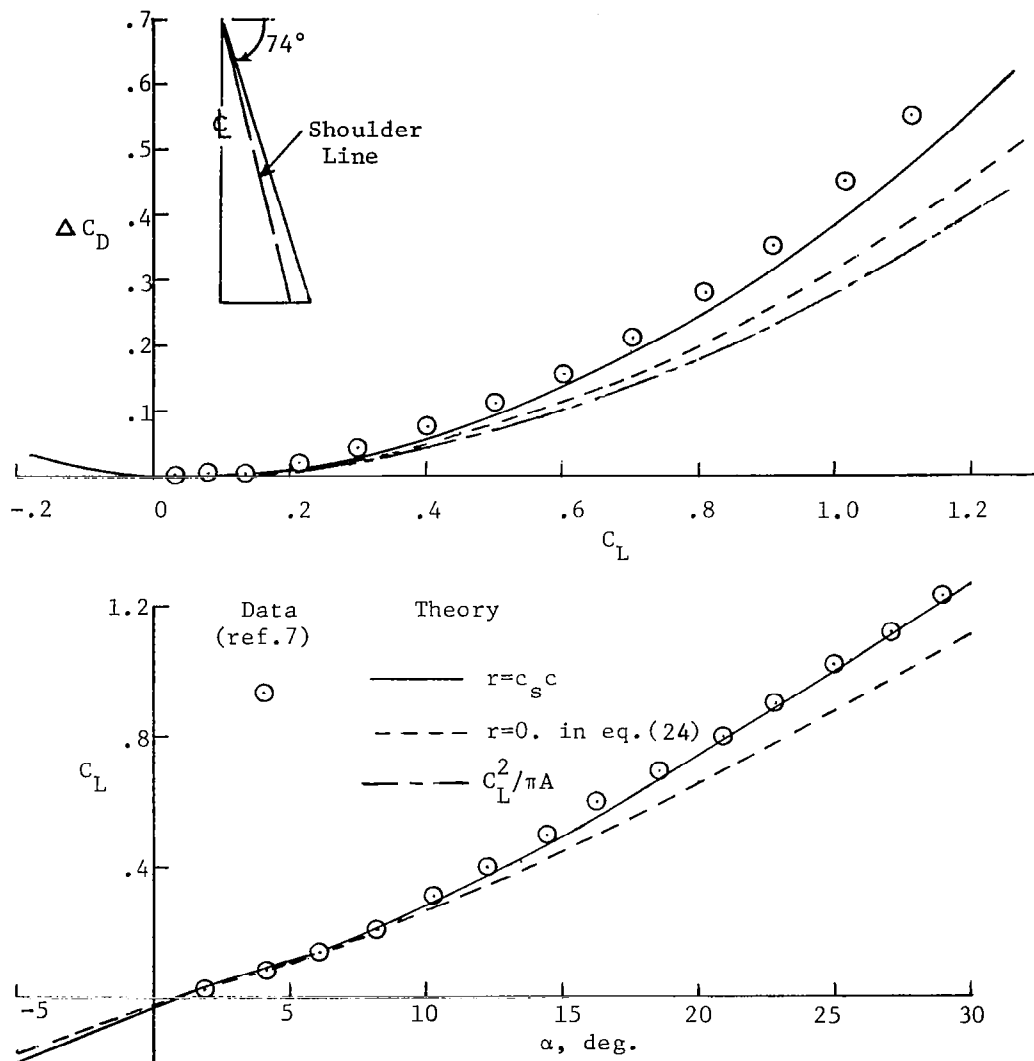


Figure 15 Effect of Vortex Lift Orientation on Predicted Aerodynamic Characteristics of  $A=1.147$  Delta Wing with Conical Camber at  $M=0$ .

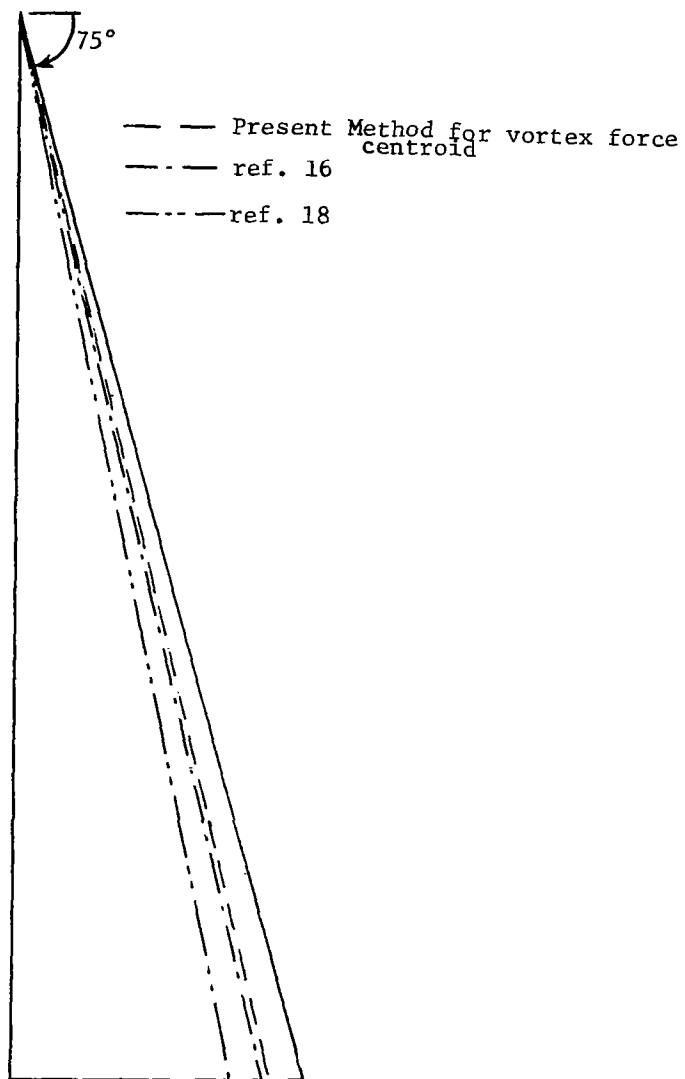


Figure 16 Vortex Locations on  $A=1.07$  Delta Wing  
at  $\alpha = 12.29$  deg.

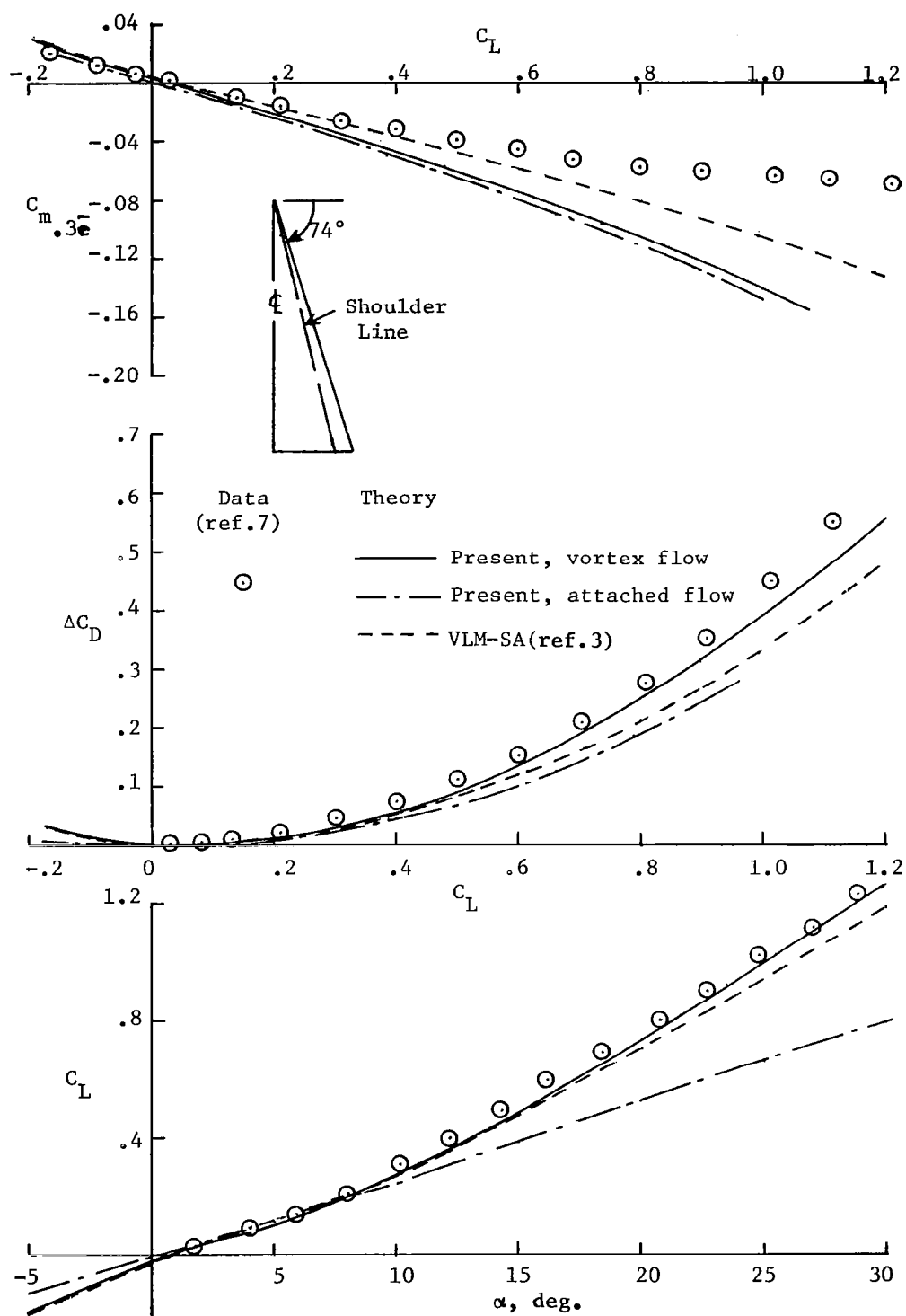


Figure 17 Aerodynamic Characteristics of  $A=1.147$  Conically Cambered Delta Wing at  $M=0$ .

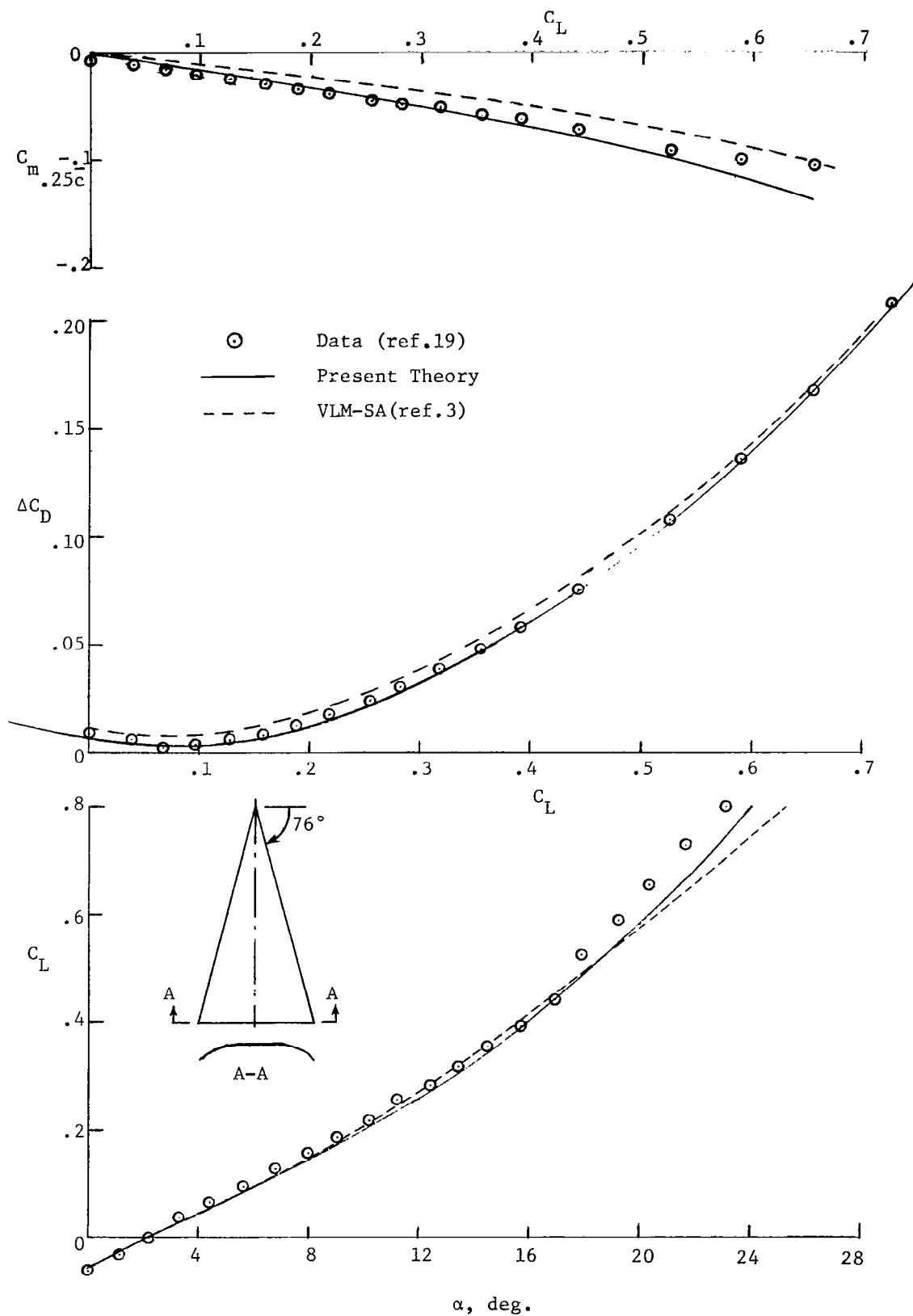


Figure 18 Longitudinal Aerodynamic Characteristics of Squire's  $A=1.0$  Cambered Wing (No.7) at  $M=0$ .

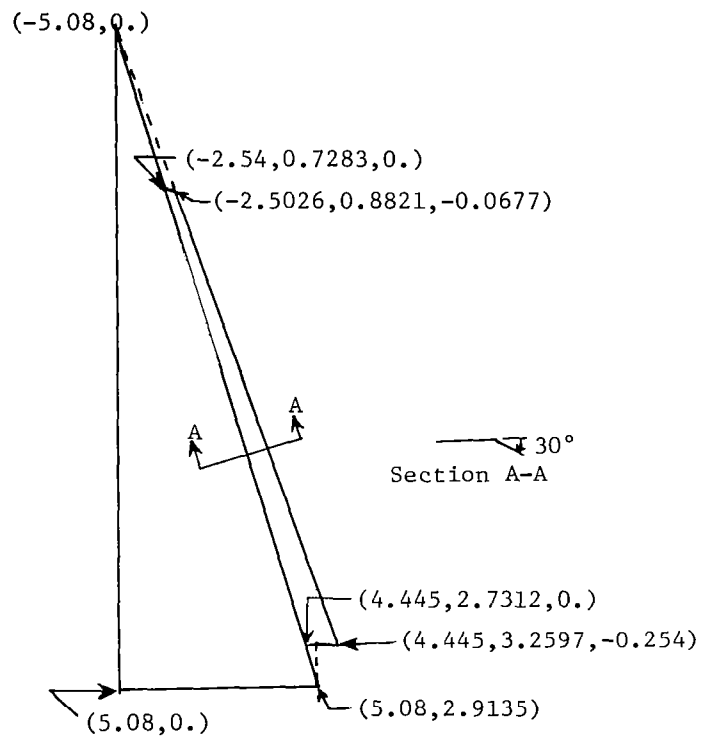


Figure 19 Geometry of a  $74^\circ$ -Delta Wing with Leading-Edge Vortex Flap Defined in Reference 8.

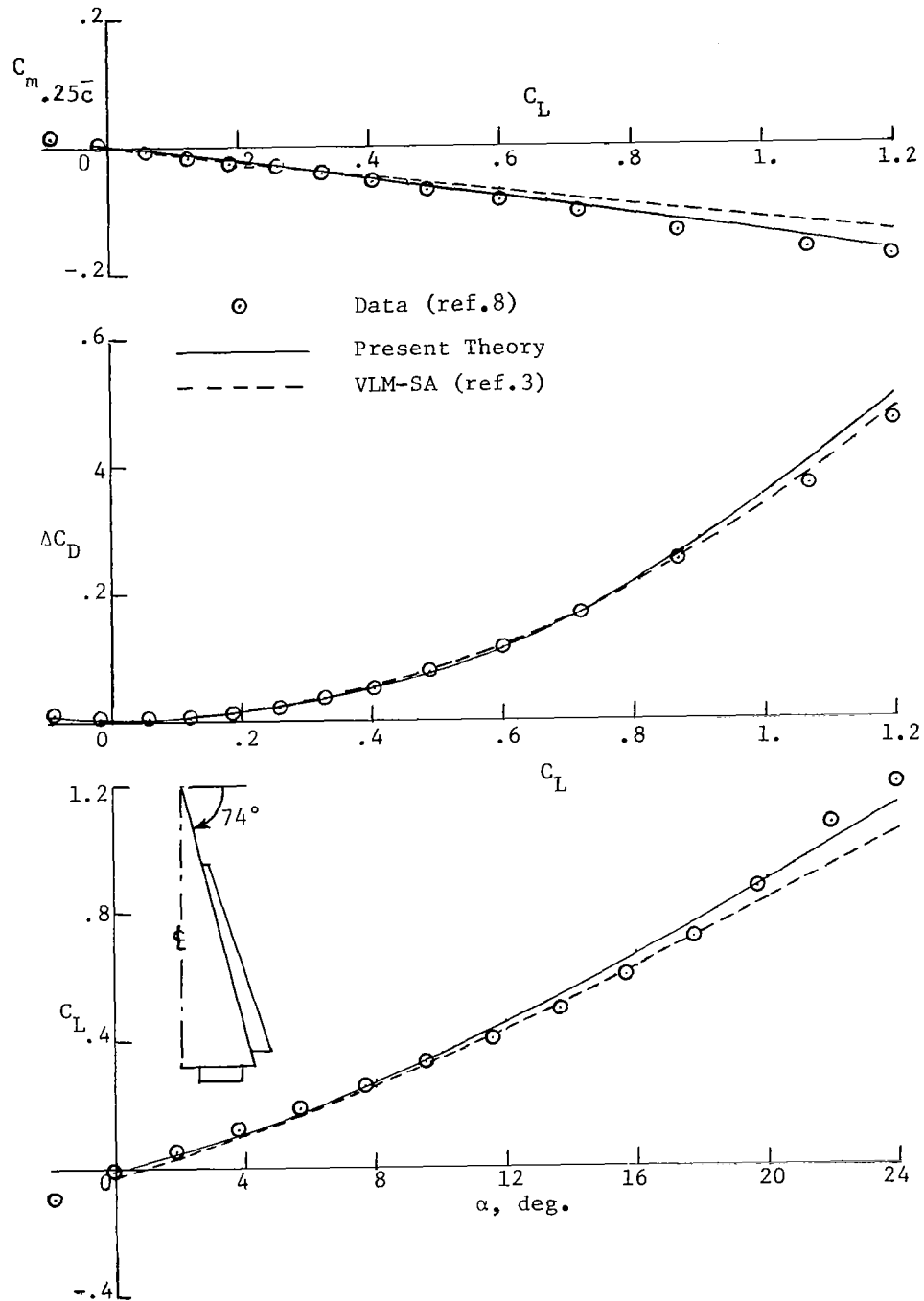


Figure 20 Longitudinal Aerodynamic Characteristics of  $A=1.147$  Delta Wing with a Leading-Edge Vortex  
Flap:  $\delta_f=30^\circ$ .  $M=0.2$

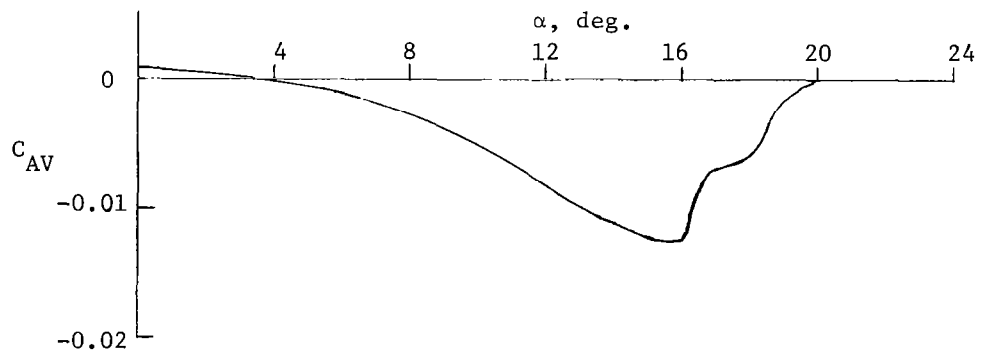


Figure 21 Axial Force Coefficient due to Leading-Edge Vortex for the 74°-Delta Wing with Leading Edge Vortex Flap by Present Method.  $M=0.2$ .

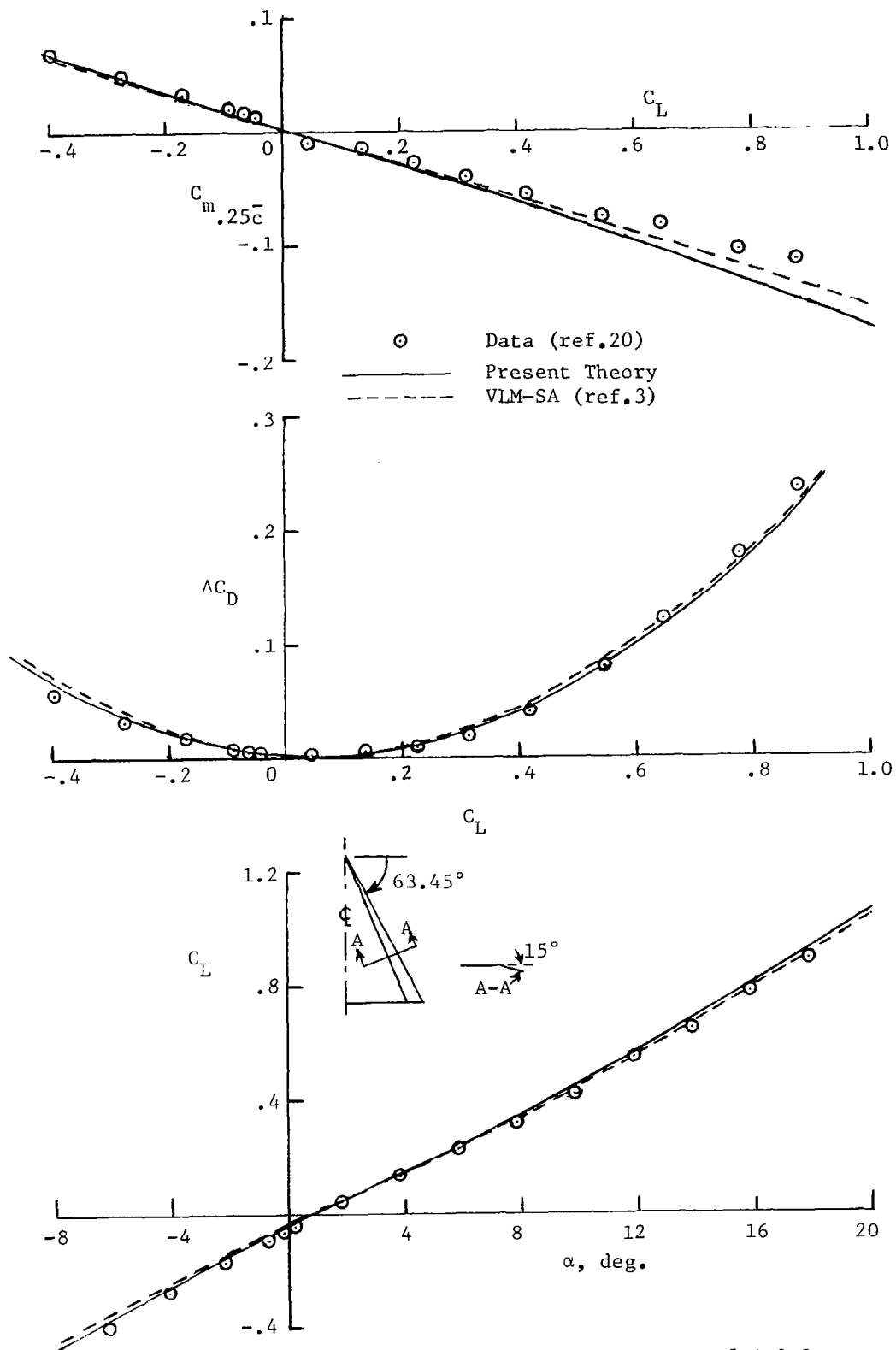


Figure 22 Longitudinal Aerodynamic Characteristics of  $A=2.0$  Delta Wing at  $M=0.7$  with Leading-Edge Flap Number 1 Deflected  $15^\circ$ .



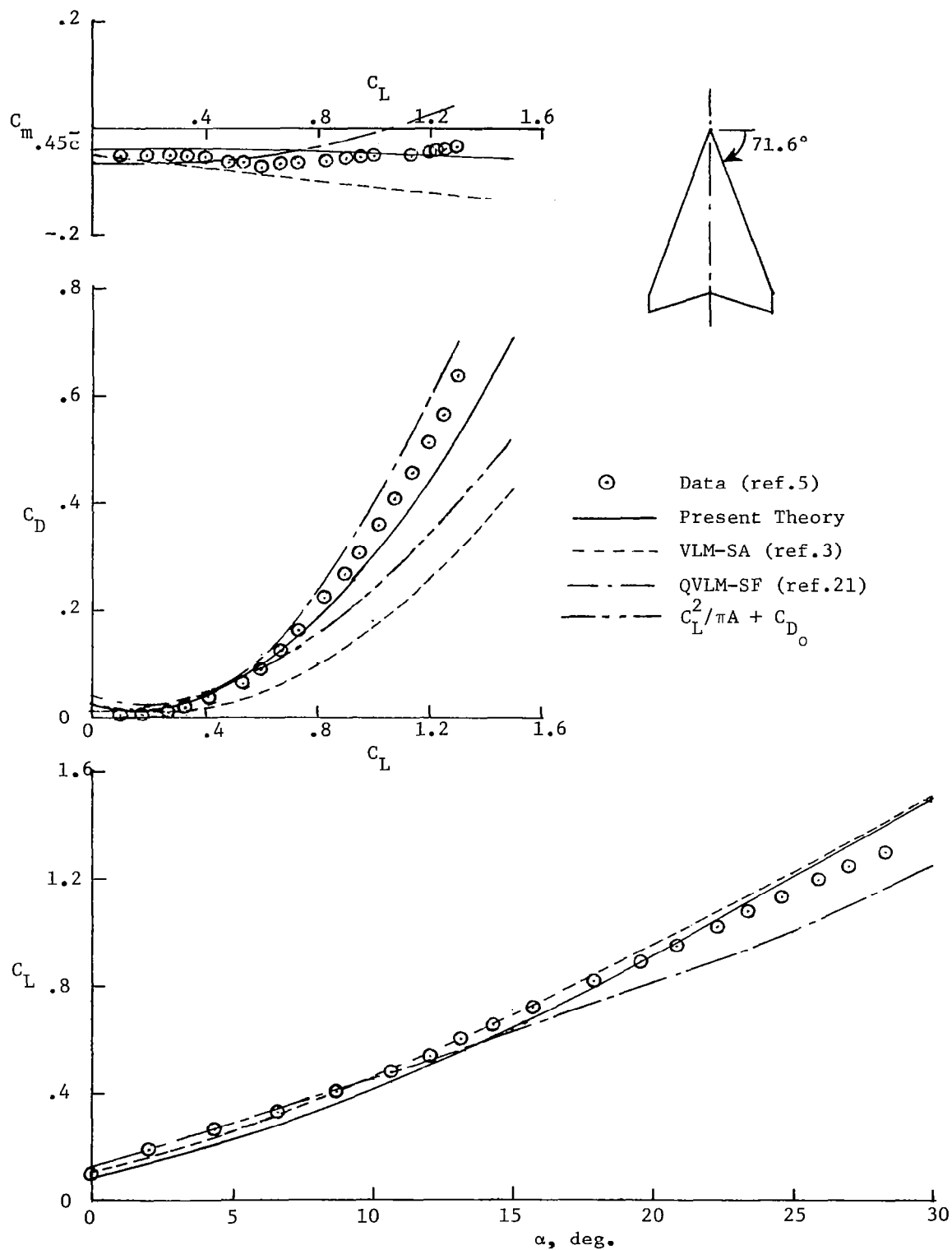


Figure 23 Longitudinal Aerodynamic Characteristics of a Cropped Arrow Wing of  $A=1.383$  and  $\lambda=0.045$  at  $M=0.6$ .

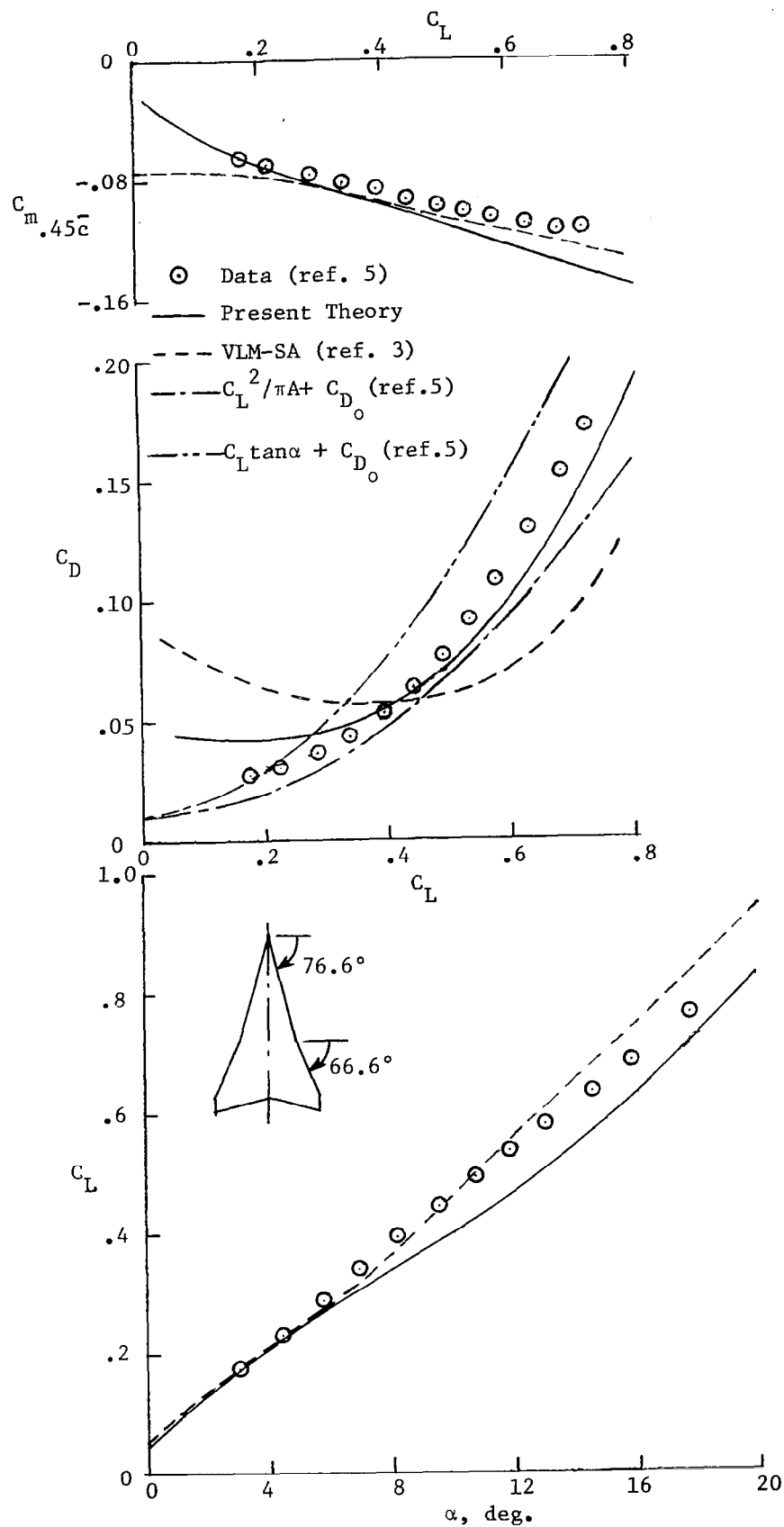


Figure 24 Aerodynamic Characteristics of A=1.383 Cranked Cambered Wing at M=0.85.

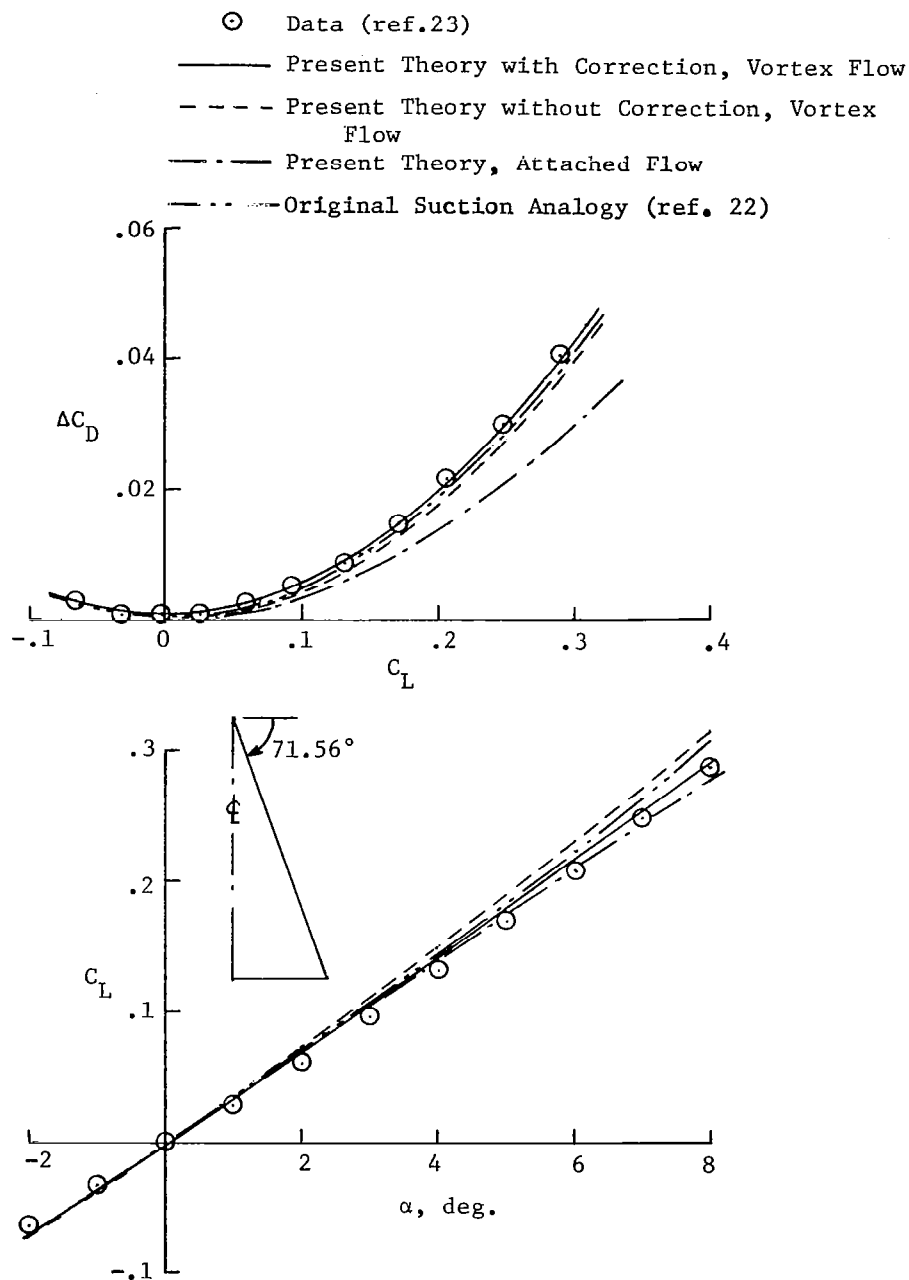


Figure 25 Aerodynamic Characteristics of a Plane  $A=1.333$   
Delta Wing at  $M=1.4$ .

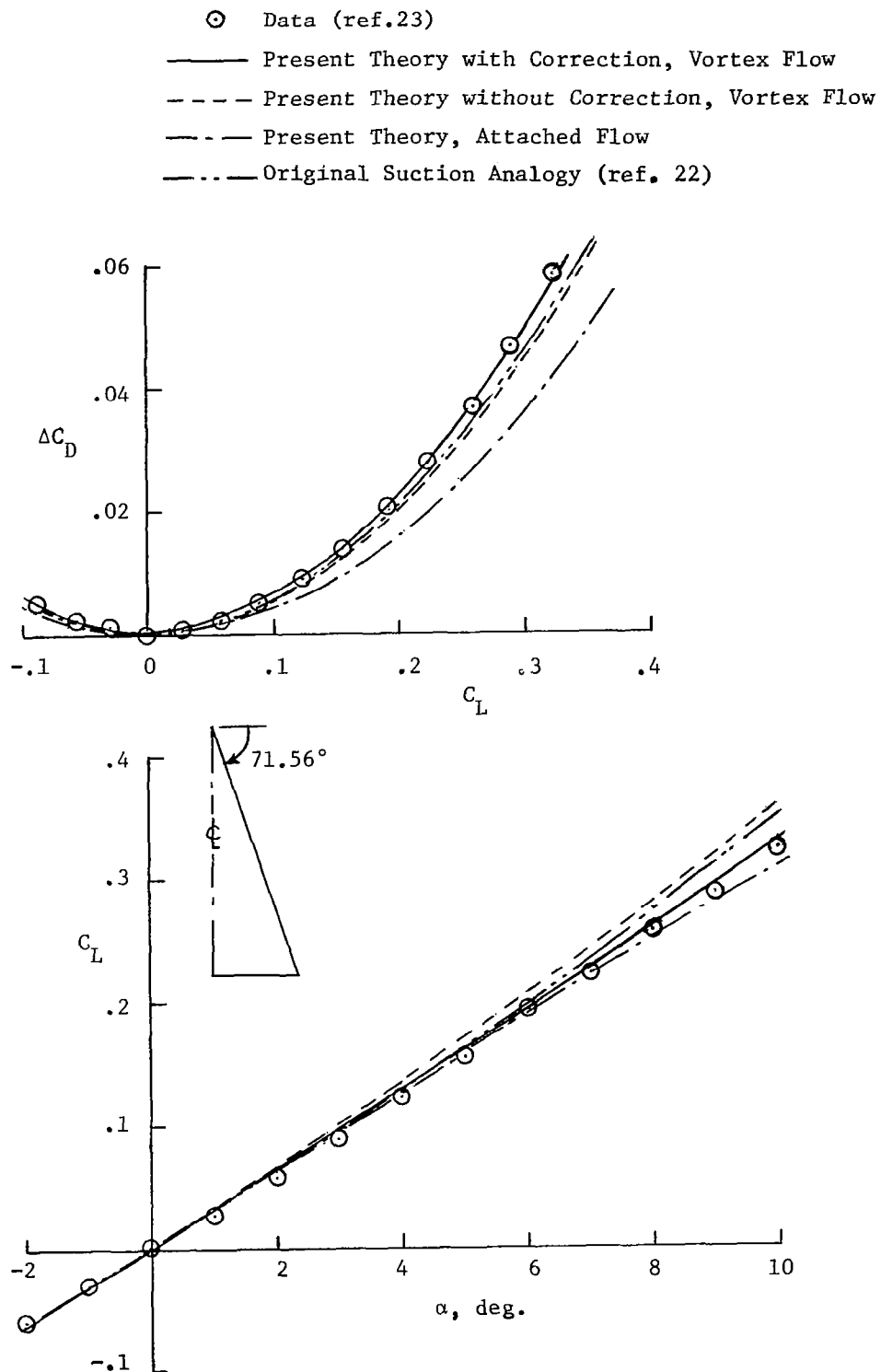


Figure 26 Aerodynamic Characteristics of a Plane  $A=1.333$  Delta Wing at  $M=1.8$ .

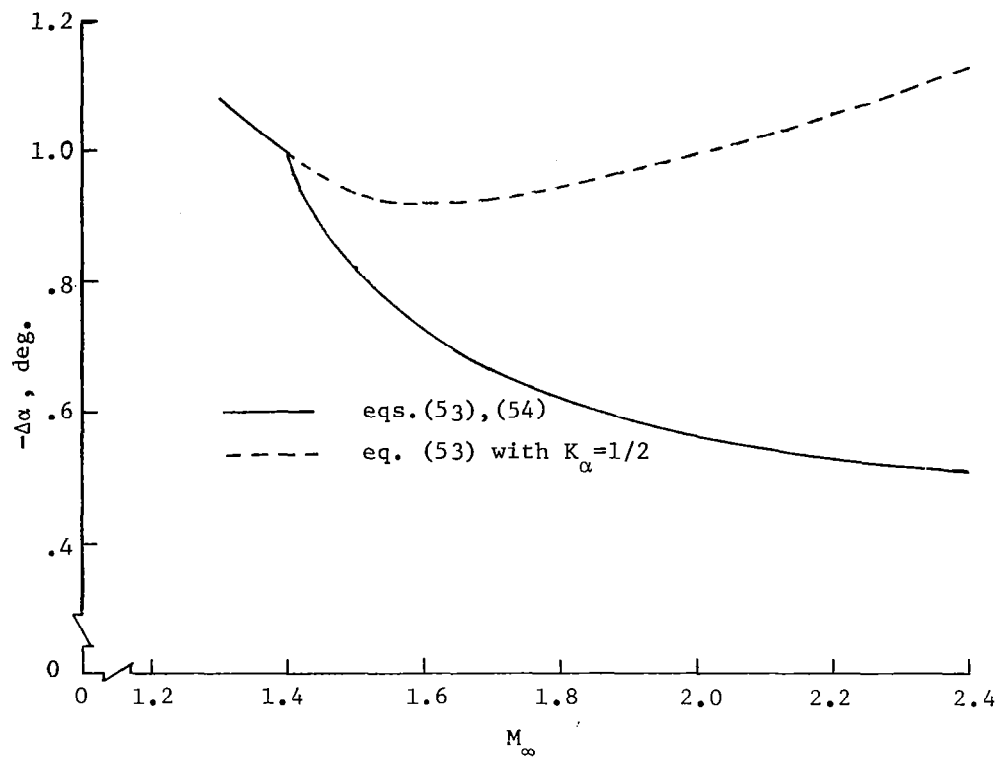


Figure 27 Angle of Attack Correction for Supersonic Vortex Separated Flow at  $\alpha=10$  deg.

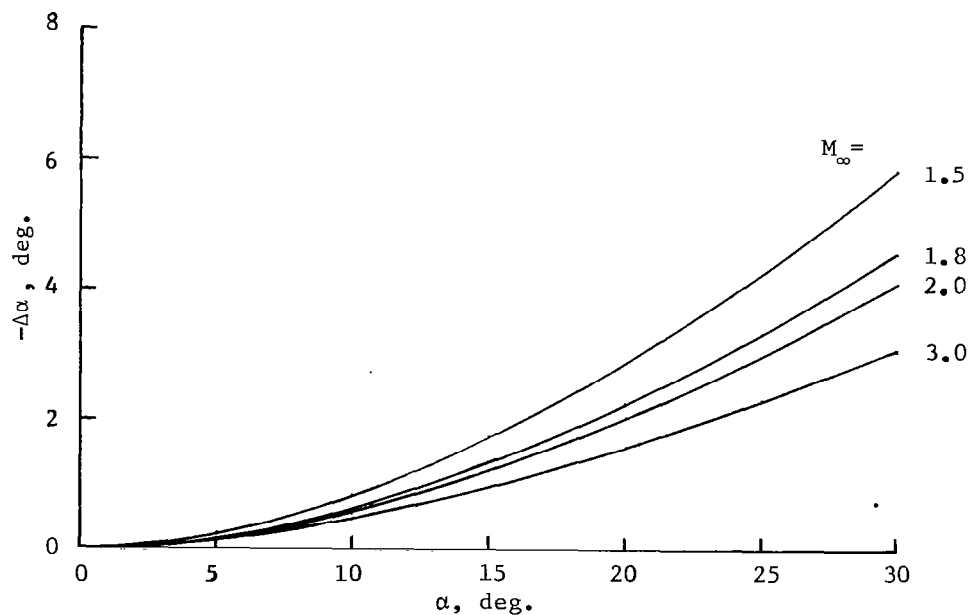


Figure 28 Angle of Attack Correction for Supersonic Vortex Separated Flow at Different  $\alpha$  and  $M_\infty$ .

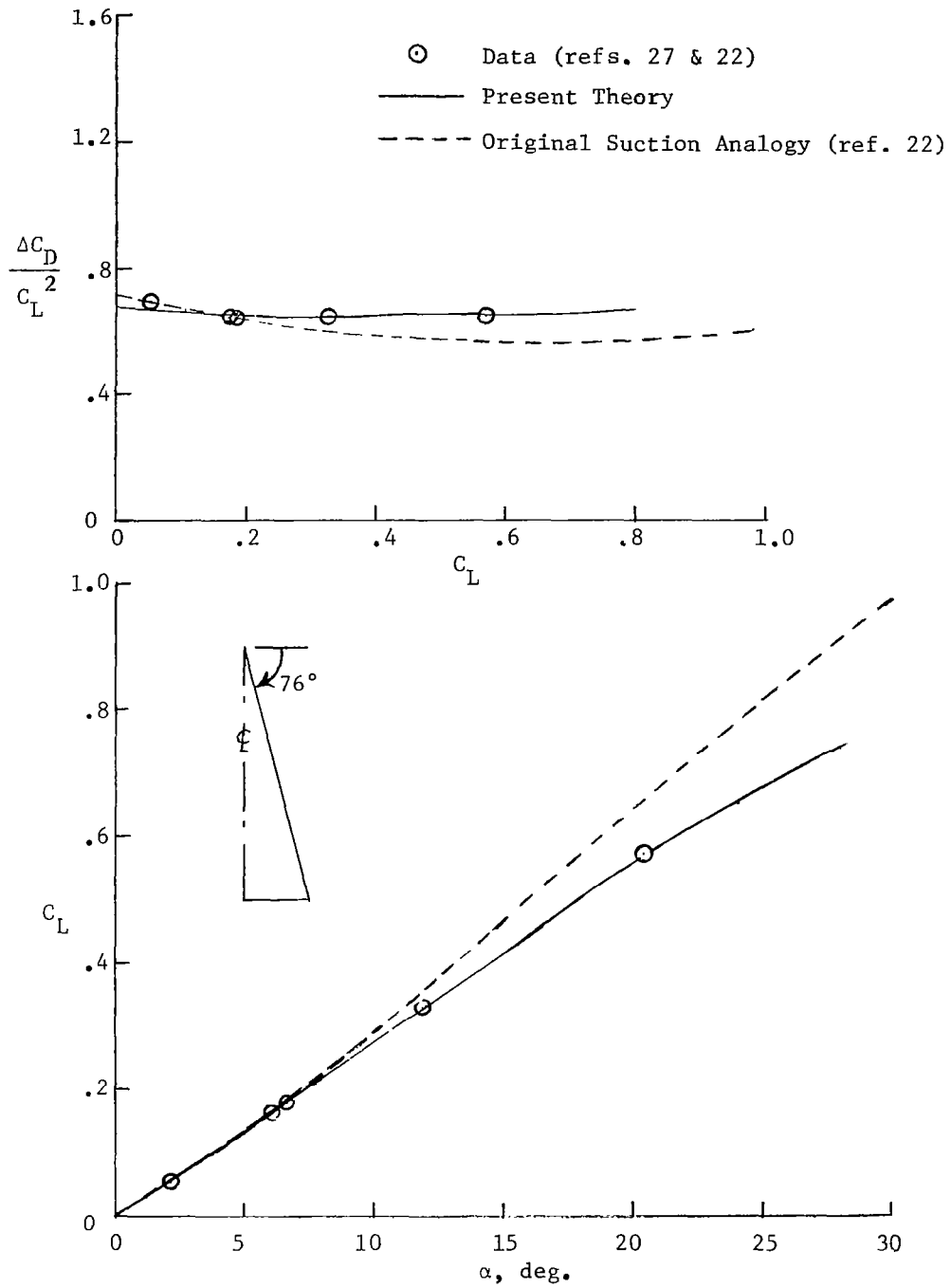


Figure 29 Aerodynamic Characteristics of A=1.0 Plane Delta Wing at M=1.97

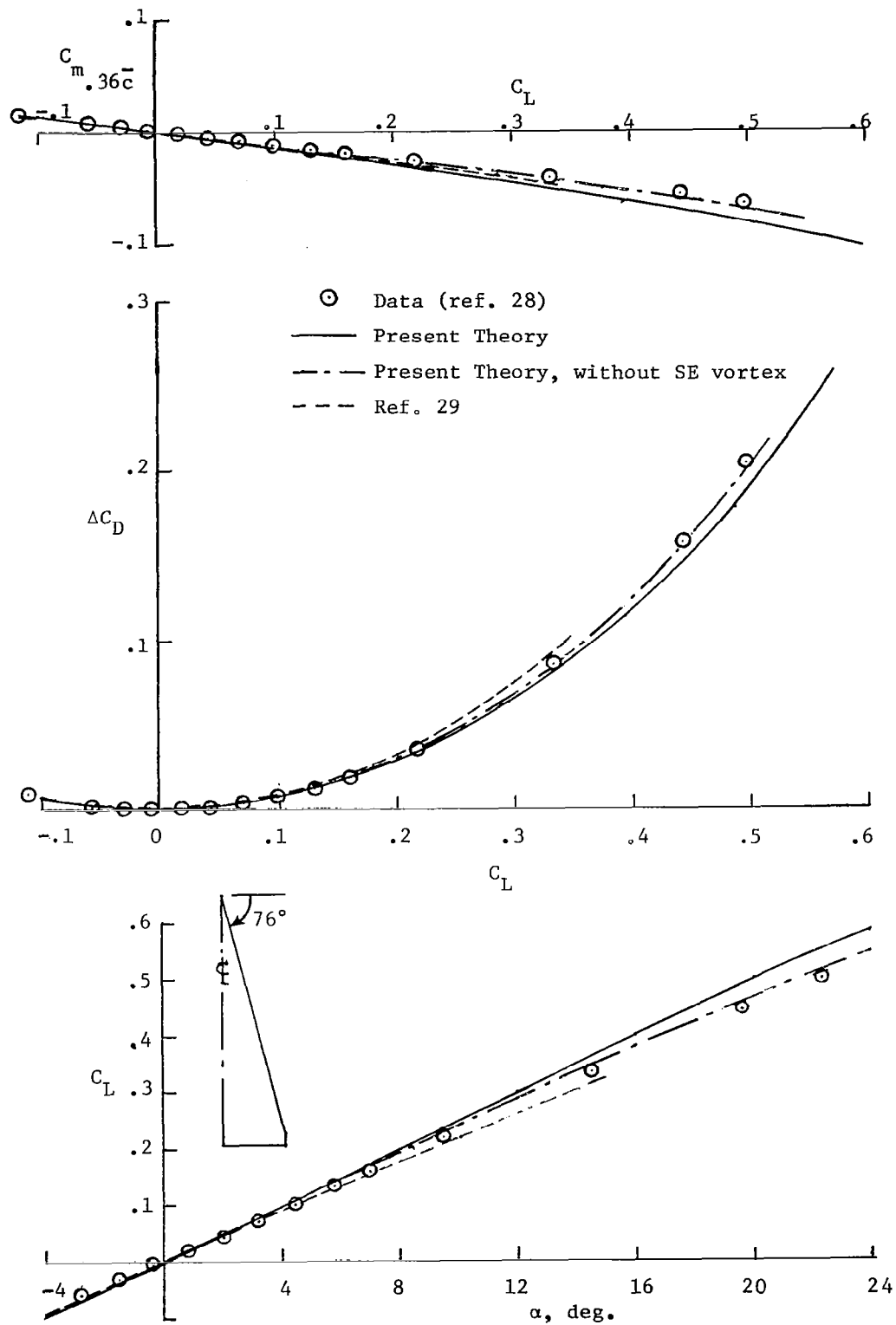


Figure 30 Longitudinal Aerodynamic Characteristics of a Cropped Delta Wing of  $A=0.9057$  and  $\lambda=0.0479$  at  $M=2.3$ .

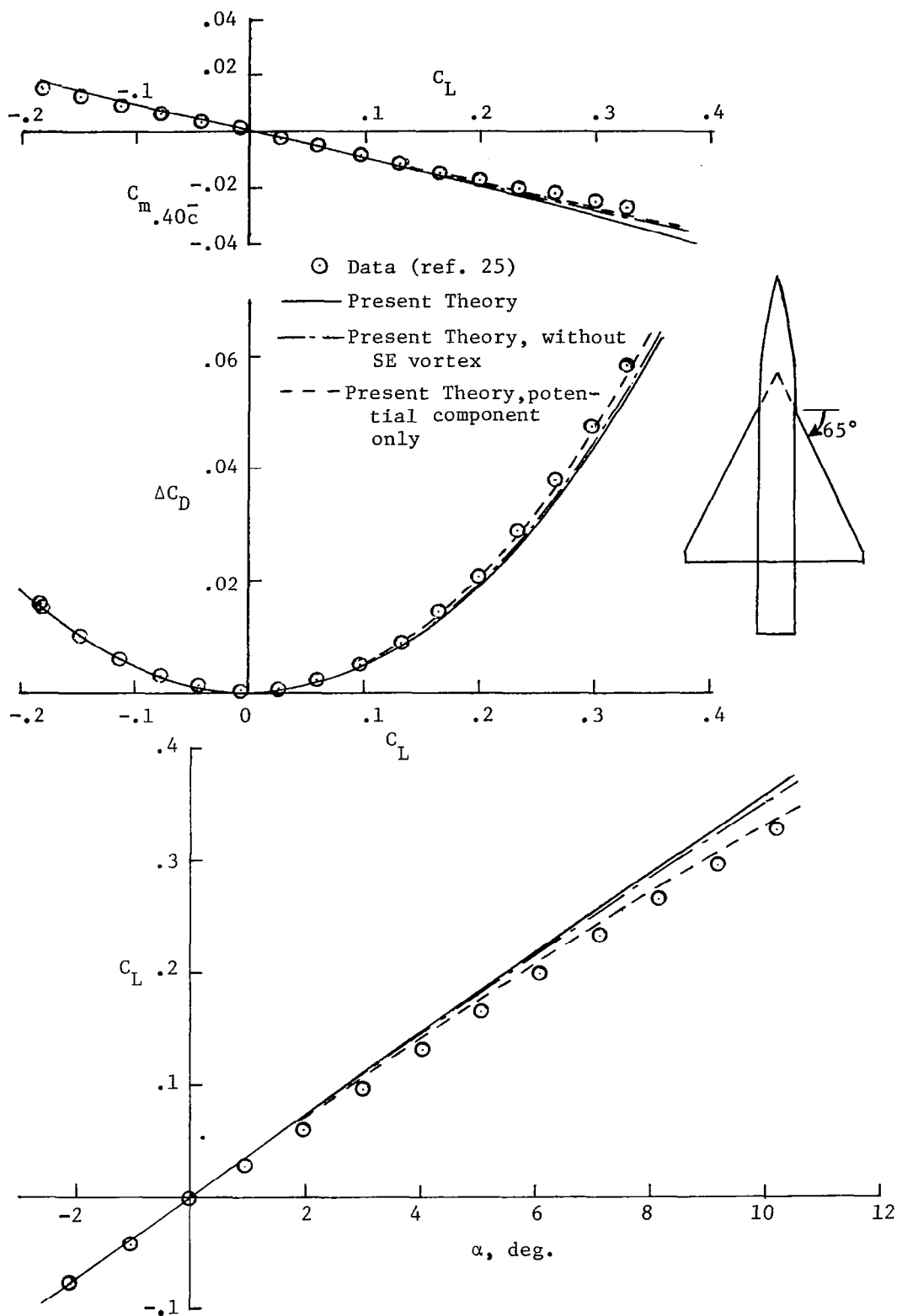


Figure 31 Longitudinal Aerodynamic Characteristics of a Cropped Plane Delta Wing of  $A=1.714$  and  $\lambda=0.045$  at  $M=2.0$ .



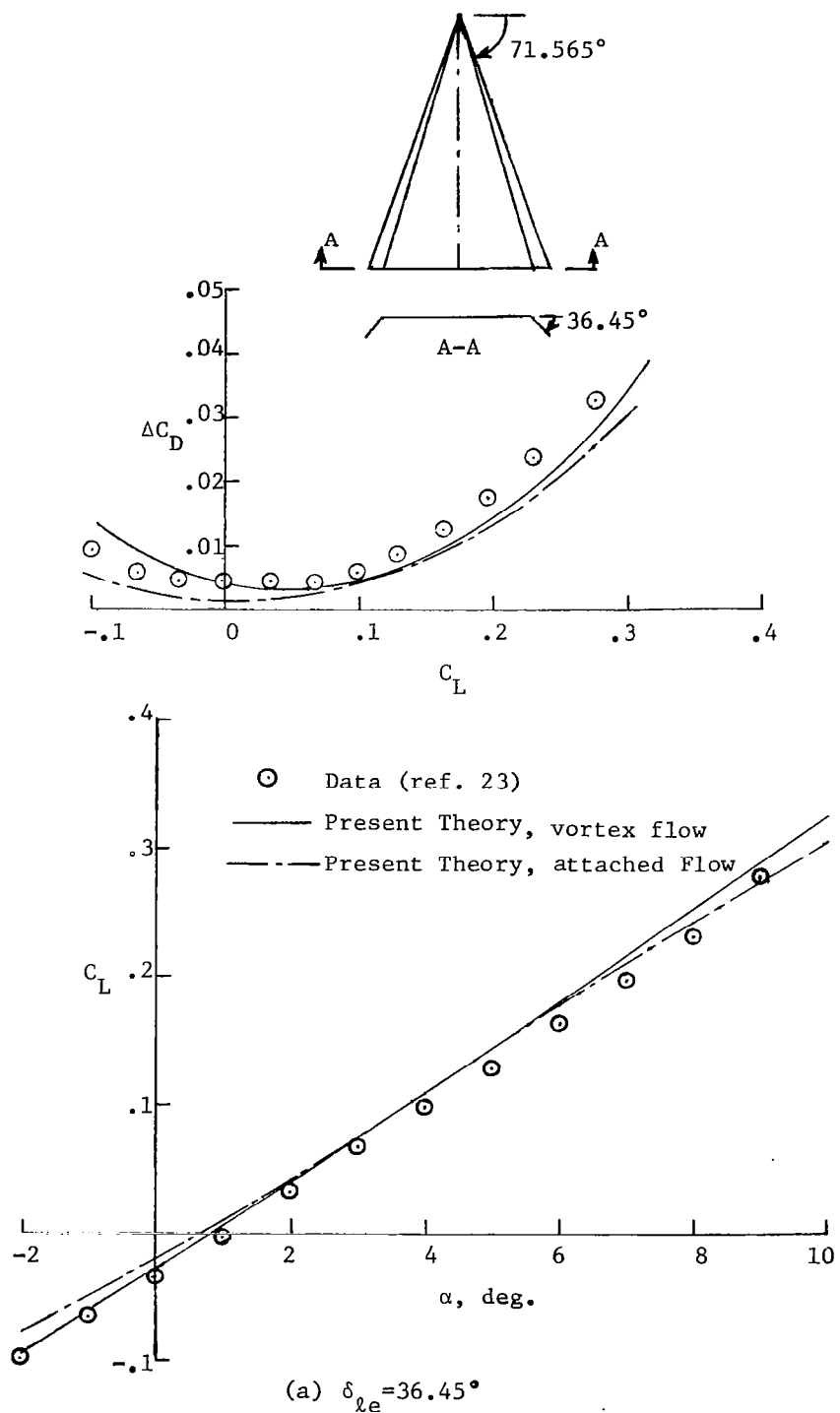


Figure 32 Aerodynamic Characteristics of  $A=1.333$  Delta Wing with Leading-Edge Flap Deflection at  $M=1.4$ .

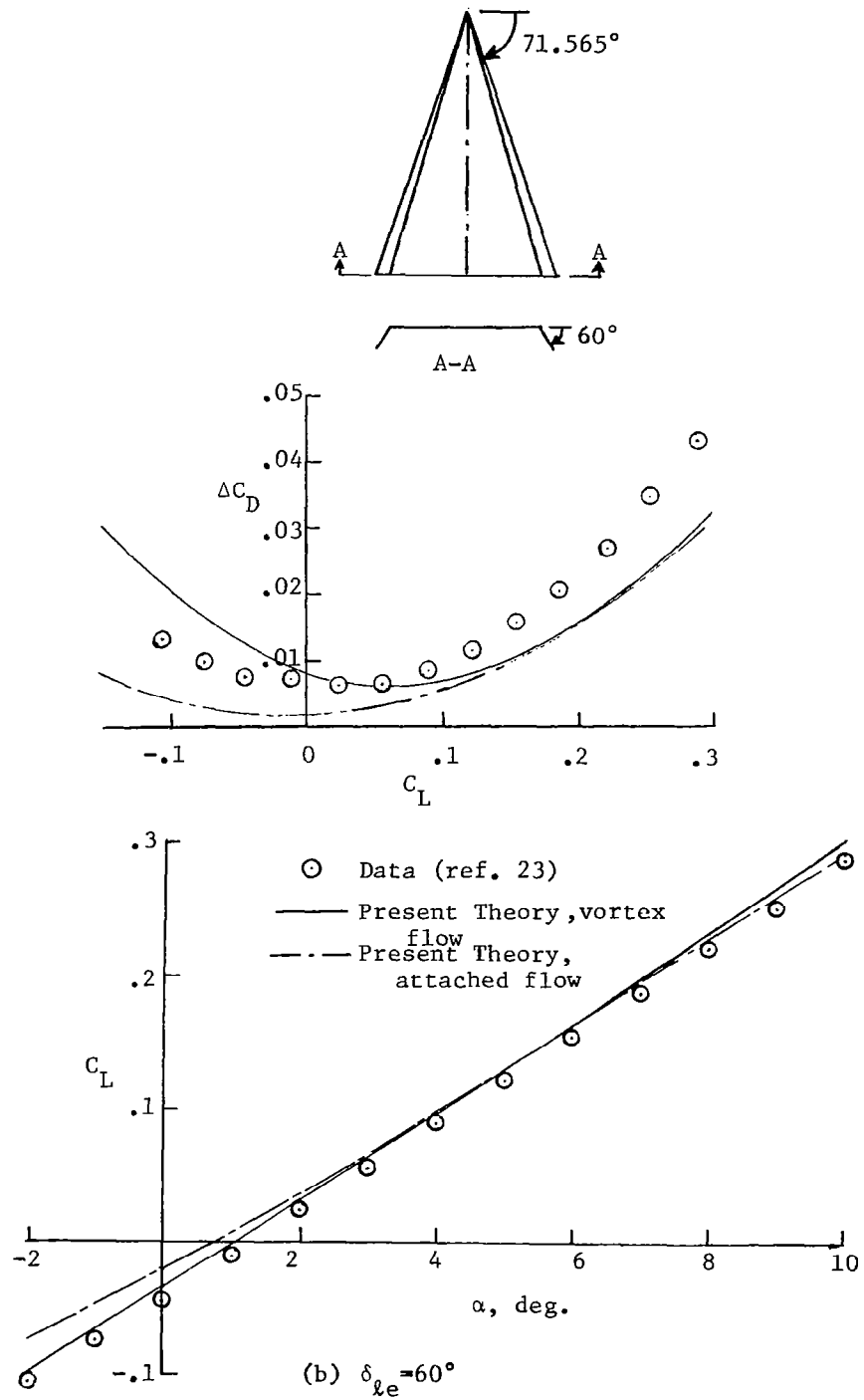


Figure 32 Concluded.

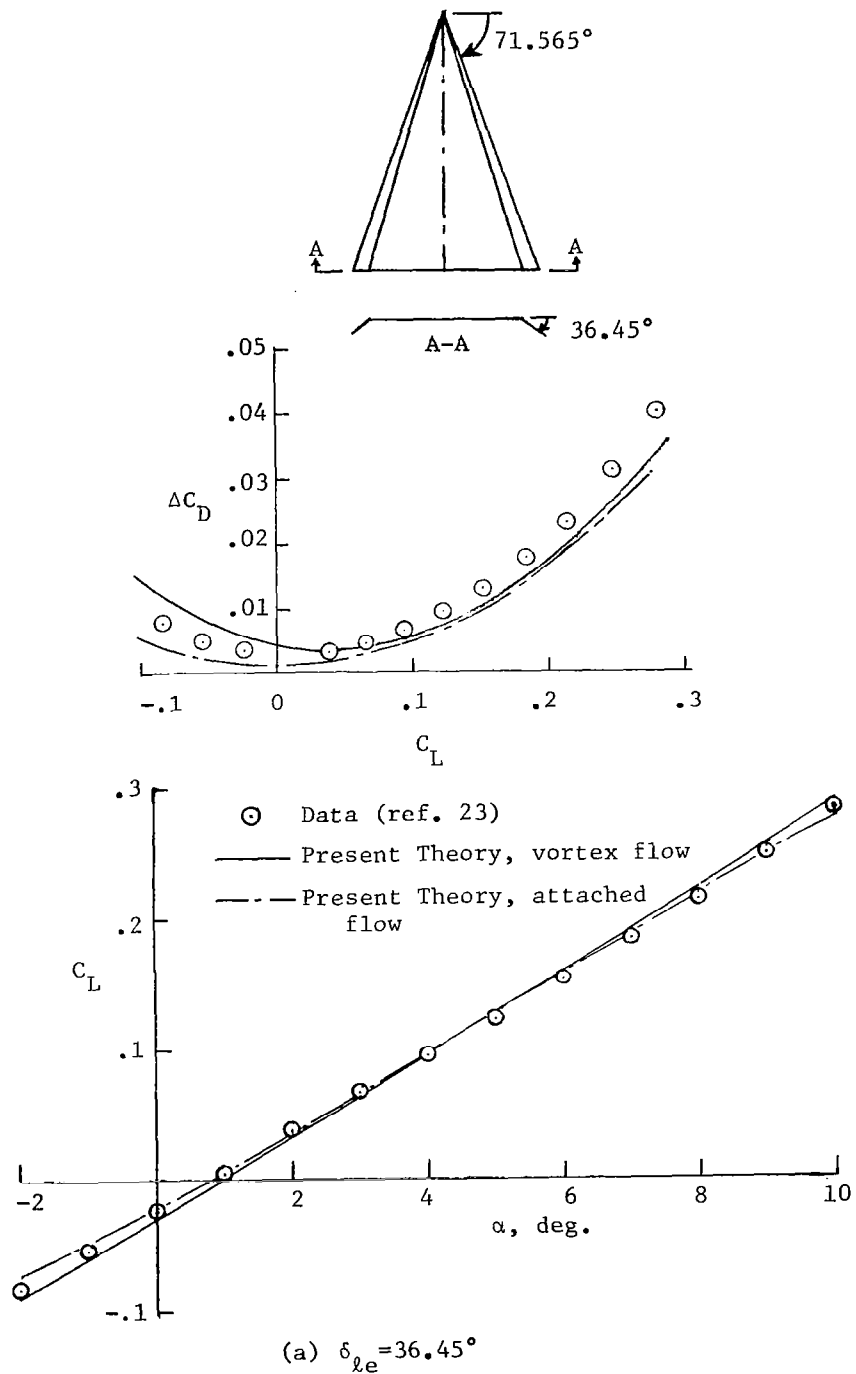


Figure 33 Aerodynamic Characteristics of A=1.333 Delta Wing with Leading-Edge Flap Deflection at M=1.8.

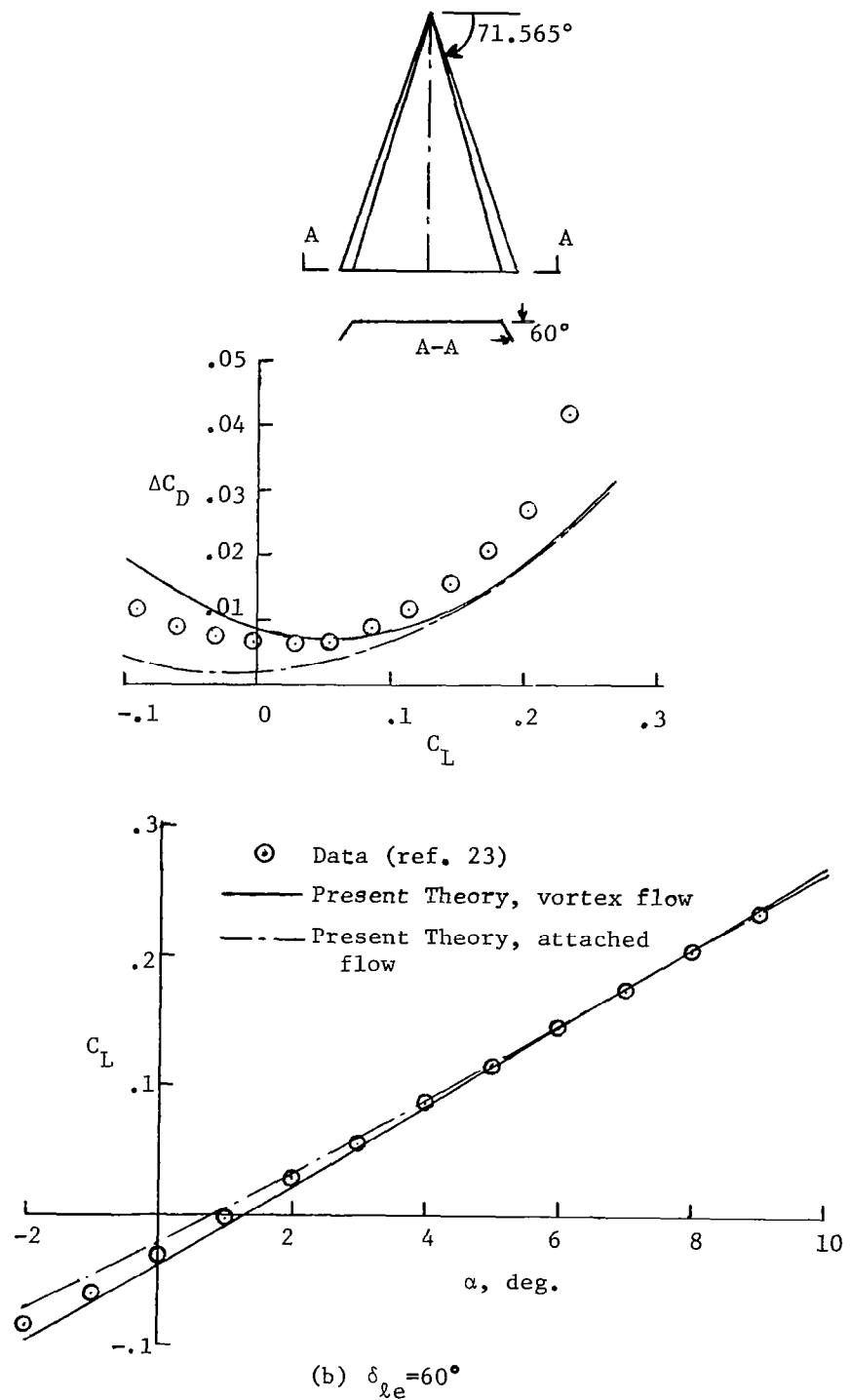


Figure 33 Concluded.

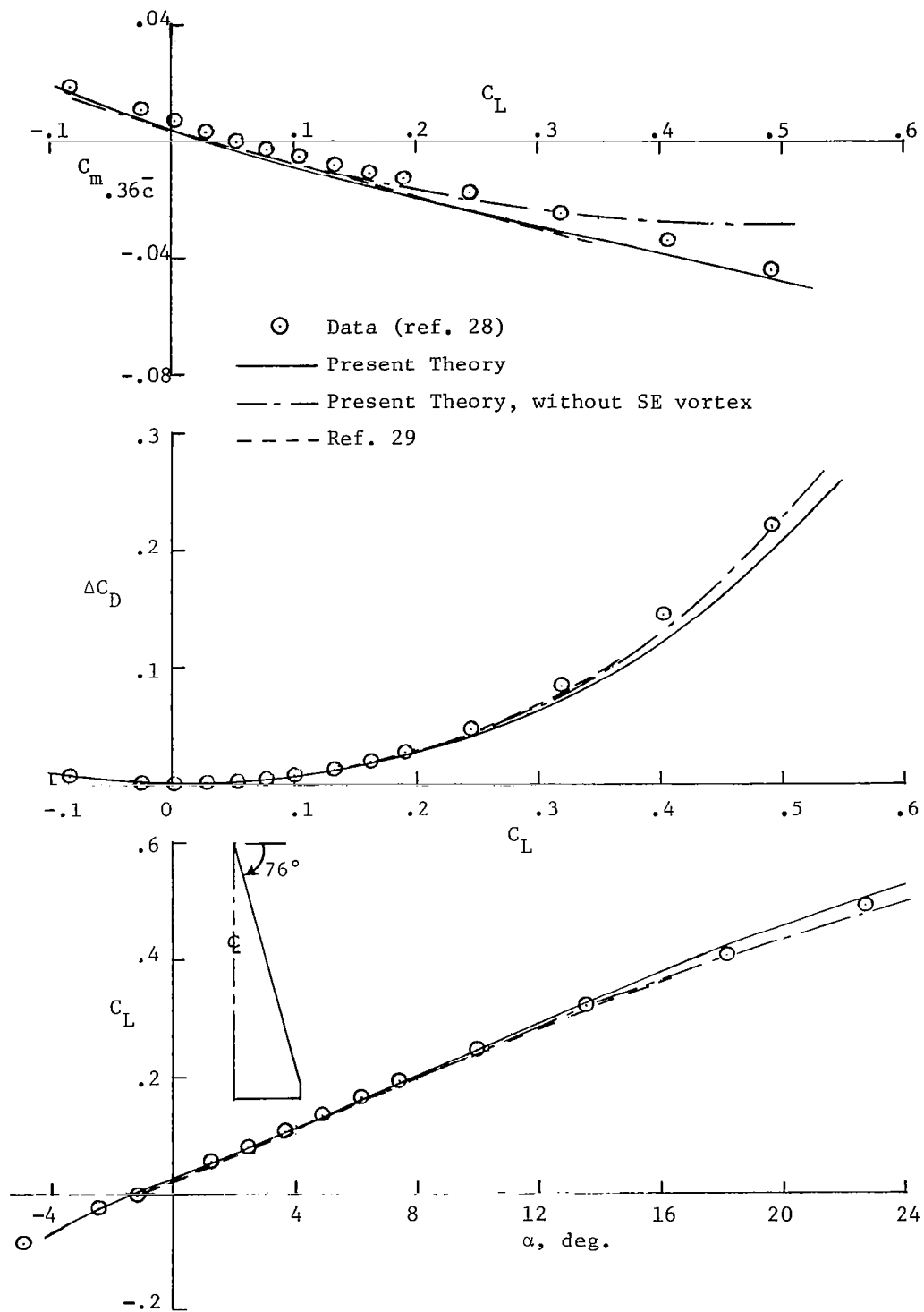


Figure 34 Longitudinal Aerodynamic Characteristics of a Cambered Cropped Delta Wing of  $A=0.9057$  and  $\lambda=0.0479$  at  $M=2.3$ .

1. Report No. NASA CR-3449		2. Government Accession No.		3. Recipient's Catalog No.	
4. Title and Subtitle CALCULATION OF VORTEX LIFT EFFECT FOR CAMBERED WINGS BY THE SUCTION ANALOGY				5. Report Date July 1981	
				6. Performing Organization Code	
7. Author(s) C. Edward Lan and Jen-Fu Chang				8. Performing Organization Report No. CRINC-FRL-426-1	
				10. Work Unit No.	
9. Performing Organization Name and Address The University of Kansas Center for Research, Inc. Lawrence, Kansas 66045				11. Contract or Grant No. NSG-1629	
				13. Type of Report and Period Covered Contractor Report	
12. Sponsoring Agency Name and Address National Aeronautics and Space Administration Washington, DC 20546				14. Sponsoring Agency Code	
15. Supplementary Notes Langley Technical Monitor: John E. Lamar Topical Report					
16. Abstract An improved version of Woodward's chord plane aerodynamic panel method for subsonic and supersonic flow has been developed for cambered wings exhibiting edge-separated vortex flow, including those with leading-edge vortex flaps. The exact relation between leading-edge thrust and suction force in potential flow is derived. Instead of assuming the rotated suction force to be normal to wing surface at the leading edge, new orientation for the rotated suction force is determined through consideration of the momentum principle. The supersonic suction analogy method is improved by using an effective angle of attack defined through a semi-empirical method. Comparisons of predicted results with available data in subsonic and supersonic flow are presented.					
17. Key Words (Suggested by Author(s)) Vortex Lift Cambered Wings Leading-Edge Suction Side-Edge Suction Subsonic and Supersonic Flow				18. Distribution Statement  Unclassified - Unlimited  Subject Category 02	
19. Security Classif. (of this report) Unclassified	20. Security Classif. (of this page) Unclassified	21. No. of Pages 84	22. Price A05		